Astron. Astrophys. 263, 258–274 (1992)

ASTRONOMY AND ASTROPHYSICS

Modelling of IR emission of interstellar clouds

I. Emission of isolated clouds and dust abundance variations

J.P. Bernard[1,3] **F. Boulanger**[1,4] **F.X. Desert**[1,2] **J.L. Puget**[1]

[1] IAS, bât 120, Campus d'Orsay, F-91405 Orsay CEDEX, France
[2] DEMIRM, Observatoire de Meudon, F-92195 Meudon, France
[3] JPL-CALTECH 320-47, Pasadena CA 91125, USA
[4] IPAC, Caltech 100-22, Pasadena CA 91125, USA

Received February 12, accepted March 9, 1992

Abstract. We have developed a general radiative transfer code for the continuum radiation to compute the incident radiation field inside a non-homogeneous, spherically symmetric cloud. We have included a dust emission model which takes into account IR emission by transiently heated small dust particles. The model has been applied to compute the emission at IR-submm wavelengths for a set of clouds of various extinction and density distributions, containing a dust composition similar to that of the diffuse interstellar medium. Although the model is not restricted to the hypothesis adopted in this paper, we assumed that the clouds are heated only by the diffuse interstellar radiation field. We give, for a wide range of density distributions and total mass, the global emission of the cloud from IR to Submm wavelengths. We also present and discuss the spatial and spectral distribution of this emission and the characteristics of the radiation field through the cloud. At IRAS wavelengths, we find that the Limb Brightening (LB) is expected to appear in all the IRAS bands if the total extinctions toward the cloud center exceeds 4-10 mag. IRAS color as 12/100 or 25/100 are predicted to decrease continuously from the edge to the center of the cloud for constant dust composition into the cloud. Comparison of these results with the IRAS data suggest that the actual color variations can only be explained by variations of dust abundance rather than by radiative transfer effects. This implies that halos with an increased abundance of small dust particles must be present around clouds showing limb brightening at short IRAS wavelengths. Possible influences of halos on the equilibrium temperature of small and bigger dust grains in dense clouds and on the associated FIR-Submm cloud emission is also investigated. The 100 μm surface brightness is predicted to be proportional to the total column density only in the outer regions of the clouds but it can be used to estimate column densities up to extinctions of $5-10$ mag if the inhomogeneities in the cloud envelope emitting most of the 100 μm radiation are small enough. For higher extinctions ($A_v > 10$ mag), the model predicts a significant LB at 100 μm which we attribute to the decrease of the temperature and emission of the bigger grains inside the cloud. As a consequence, the 100 μm surface brightness is limited to $\simeq 20$ MJy/sr for any model, independent of column density. In the FIR-Submm, the LB effect progressively disappear and the global emission of the cloud becomes progressively proportional to its mass.

Key words: molecular clouds – radiative transfer – dust – infrared radiation

Send offprint requests to: J.P. Bernard

1. Introduction

Results of the sky survey by the Infra-Red Astronomical Satellite (IRAS) at 12, 25, 60 and 100 μm have revealed the existence of an excess in the shortest wavelength bands (12, 25 and 60 μm) relative to the predictions from models where all the IR emission is coming from dust grains in thermal equilibrium with the incoming radiation field. The excess can be explained, if dust particles that are small enough to experience important temperature fluctuations when receiving UV photons, participate to the IR emission, their temporary high temperature giving rise to the observed IR excess. Several hypotheses have been formulated, regarding the possible chemical nature and optical properties of this new dust component. Models using silicate-graphite mixtures of the type introduced by Mathis, Rumpl, Nordsieck 1977 but extended toward small particle sizes generally predict too much extinction in the 2200 Å bump of the extinction curve compared with the additional emission produced at 12 μm (Draine & Anderson 1985). A model in which the IRAS 60 μm is attributed to emission by iron grains that can, under the same excitation conditions, reach higher temperatures than graphite or silicate grains with the same size has also been proposed (Chlewicki & Laureijs 1988) but also requires small dust particles to produce the observed intensities in the shorter wavelength bands.

The family of IR emission features at 3.3, 6.2, 7.7, 8.6 and 11.3 μm observed in various astrophysical environments have been identified with emission from the vibrational modes of Polycyclic Aromatic Hydrocarbon (PAH) molecules (Léger & Puget 1984, Allamandola et al. 1985). This dust component can be interpreted either as big molecules or as extremely small, 2-dimensional dust grains experiencing violent temperature fluctuations followed by IR emission in vibrational desexcitation channels (Léger & Puget 1984, Allamandola et al. 1985). The

recent detection of the 3.3 μm extended emission of the galactic plane (Giard et al. 1989) is also one more indication that very small dust particles with fluctuating temperatures emitting in the NIR could be an ubiquitous component of the dust in the Galaxy. Evidence has also been gathered that these small particles could be an important component in external galaxies as well (Helou, Ryter and Soifer 1991). It is therefore justified to assume a continuous size distribution of the dust from PAH sizes (3 Å) to classical big grains in thermal equilibrium (0.1 μm).

A recent model proposed by Desert, Boulanger and Puget (1990, DBP) has shown that the average properties for both extinction and IR emission of the local diffuse ISM can be reproduced with a dust composition which consist of three families of dust particles: PAH, Very Small Grains (VSG) and Big Grains (BG). The components have optical properties consistent with available laboratory data (e.g. Léger et al. 1989). In the DBP model, under solar neighborhood excitation conditions, a significant fraction of the energy output in the 12 μm IRAS band is due to the contribution of the PAH 7.7 and 11.3 μm emission features as well as a quasi-continuum due to weaker features in this band. PAH also contribute a significant fraction ($\simeq$ 48 %) of the emission in the 25 μm band emission. BG are composed of a silicate core covered by a carbonaceous coating and have a flat extinction in the UV. Their emission dominates the emission in the 100 μm band. Intermediate size particles are assumed in this model to be Very Small 3-D Grains (VSG) of carbonaceous (e.g. graphite) material producing the extinction bump at 2200 Å. Their presence in the ISM is required in order to explain the continuous spectrum between 25 and 100 μm (52 % and 60 % of the total emission in the 25 and 60 μm bands respectively).

Another feature exhibited by the IRAS data is the Limb Brightening (LB) of isolated molecular clouds in the short wavelength IRAS bands. This effect has been noticed in the case of the cloud Barnard 5 by Beichman et al. (1988) as an increase of the 12 and 25 μm emission at the edge of the cloud relative to the center. The same effect was also noticed by Laureijs et al. (1989) in a $A_V \simeq$ 1.8 mag extinction cloud (G299-16) of the Chamaeleon complex at 12 and 25 μm. It has also been reported at various scales in various molecular complexes (Boulanger et al. 1989 and Puget 1989). The same effect has also been observed for the 60 μm intensity distribution (Laureijs et al. 1991) in a dark cloud (L134) with a substantially higher extinction of $A_V \simeq$ 10 mag. Possible explanations for the observed brightness increase near the edge of the cloud is that the dust emissivity in the short IRAS wavelengths is strongly reduced in the internal regions where most energetic UV photons, responsible for the sporadic heating of the very small dust particles, have disappeared. The 100 μm emission, mainly due to thermal emission by bigger grains that can be heated by lower energy photons, does not present such a feature and is therefore proportional to the dust column density in the cloud. As the IR emission in the various IRAS bands seems to be produced by dust particles of different sizes, the LB effect could also be due to real variations of the abundances of particles with different sizes across the cloud.

In order to quantify the importance of the LB effect due to radiation attenuation, we have included the dust model proposed by DBP into a radiative transfer code for the continuous heating radiation in a spherically symmetric, non homogeneous cloud heated by an external isotropic Inter-Stellar Radiation Field (ISRF) expected for the solar neighborhood. This model uses the optical properties of each dust components of the DBP model and has been used to predict the expected IRAS brightness profiles for various clouds with low to moderate extinctions ($0 < A_V < 50$ mag). As extinction and emission are treated self-consistently in the model, it is possible to investigate selective variations of certain dust components in the cloud. We also considered a few higher extinction clouds (100-500 mag).

In Section 2, we describe the model used. Only the radiative transfer part is described, as the local dust emission calculations and dust optical properties are exactly similar to the one described in DBP. In Section 3, we present the results for a series of clouds with various extinctions and density distribution, with an homogeneous and standard chemical composition of the dust across the cloud and heated only by the external ISRF. These results are discussed in Section 4 and compared to results from other models and IRAS data for some clouds. We also present in this Section results for models with a non homogeneous PAH abundance in the cloud. Section 5 is the conclusion.

2. Model description

2.1. Radiative transfer

We have developed an iterative method using a layer model to compute the radiative transfer in a spherical, non homogeneous cloud isotropically heated by the ISRF. We represent the cloud by a succession of concentric layers with variable thickness $\Delta r(i)$. The geometry of the model is presented in Fig. 1. The gas density $\tilde{n}_H(i)$ and dust abundances and properties are fixed in each layer but can vary from one layer to the other. For all the radiative transfer calculations, the optical depth of each layer is computed according to the dust composition in each layer using the optical properties given in DBP for each specie.

The diffusion of UV photons, which, in the frame of this dust model, is mainly due to one dust component (BG) is not taken into account explicitly here. We assumed instead that all the diffusion processes are completely forward (ie, the mean cosine of the scattering angle $g = 1$) and used accordingly a pure absorption cross section in radiative transfer calculations. Possible consequences of this approximation are discussed in Section 4.

Using the spherical symmetry, the incident spectrum integrated over angles due to the ISRF at the center $r(i)$ of each layer i is computed as:

$$(4\pi I_\nu)_{\mathrm{ISRF}}(i) = \frac{1}{2}(4\pi I_\nu)_{\mathrm{ISRF}}(r_m)\int_{-1}^{+1} e^{-\tilde{\tau}_\nu^e(u)}du, \quad (1)$$

where $(I_\nu)_{\mathrm{ISRF}}(r_m)$ is the ISRF specific intensity at the edge of the cloud of radius r_m. $\tilde{\tau}_\nu^e(u)$ is the optical depth at frequency ν from the center of layer i to the outside of the cloud along the direction defined by $u = \cos(\theta)$ (see Fig. 1). $\tilde{\tau}_\nu^e(u)$ is computed by summing over all the layers crossed along the direction u from the center of layer i:

$$\tilde{\tau}_\nu^e(u) = \sum_j \sigma_\nu^H(j)\tilde{n}_H(j)\tilde{L}_j(u), \quad (2)$$

$\tilde{L}_j(u)$ is the length through layer j along this direction. $\sigma_\nu^H(j)$ is the cross section per H atom of the dust mixture in layer j. Given the first order estimate of Eq. (1) for the incident radiation field, the IR dust emissivity $\epsilon_\lambda^o(i)$ per unit length ($\epsilon_\lambda^o(i) = dI_\lambda/dl$) is calculated in each layer using the DBP model. For subsequent steps of the iterative procedure, we re-compute the radiation field in each layer, adding the diffuse IR contribution from all the other layers integrated over directions:

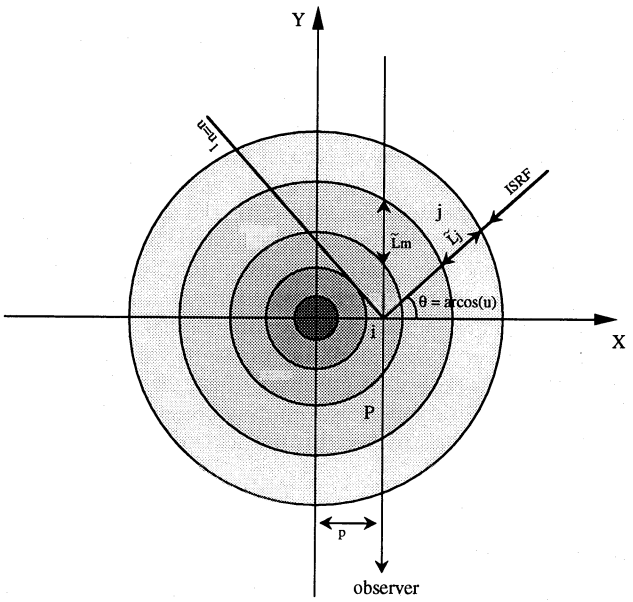

Fig. 1. Schematic representation of the layer model used to compute the radiative transfer in a spherical non-homogeneous cloud. The incident radiation field at the center $r(i)$ of layer i is computed by integrating over directions $u = \cos(\theta)$ both the external ISRF and the diffuse IR heating contributed by all the other layers of the model. Optical depths and IR emission on direction u are computed using the distances of the type $\tilde{L}_j$. Integration over the line of sight with offset $p = r(i)$ from the center is computed by summing all the contributions using $\tilde{L}_m$ and the IR optical depth from the considered layer m to the observer

$$(4\pi I_\nu)^{\circ}_{\rm dust}(i) = 2\pi \int_{-1}^{+1} \sum_j e^{-\tilde{\tau}^{ij}_\nu(u)} \epsilon^{o}_\lambda(j) \tilde{L}_j(u) {\rm d}u, \quad (3)$$

where the sum is over all layers along the direction u from the center of layer i and $\tilde{\tau}^{ij}_\nu(u)$ is the optical depth between the center of layer i and j along this direction as in Eq. (2). Due to the spherical symmetry, $(4\pi I_\nu)_{\rm dust}$ is constant in each layer. A new value of the IR dust emissivity $\epsilon^{1}_\lambda(i)$ is computed using the total incident spectrum $(4\pi I_\nu)^{\circ}_{\rm dust} + (4\pi I_\nu)_{\rm isrf}$ which includes a first order estimate for the IR contribution to the heating and so on. At each step k of this iterative procedure, the emerging spectrum of the cloud along each line of sight is derived as a function of the impact parameter p relative to the cloud center:

$$I_\lambda(p) = \sum_m \epsilon^{k}_\lambda(m)\, e^{-\tau_\nu(u_p)} \tilde{L}_m(u_p), \quad (4)$$

where the sum is taken over layers with $r(j) \geq p$ and $\tau_\nu(u_p)$ is the optical depth from the center of layer j to the observer along the line of sight. The corresponding total power P_k emitted by the cloud as a whole is compared to $P_{\rm abs}$, the total power absorbed by all the dust present in the cloud when only the ISRF radiation is taken into account. For $k = 0$, $P_k < P_{\rm abs}$ because the IR absorption by dust along the line of sight is taken into account to compute P_k (Eq. (4)) but not yet as an explicit heating source for the dust. When iterations over IR heating are performed, P_k then converges toward $P_{\rm abs}$. The iterations are stopped when $P_k \simeq P_{\rm abs}$. We must note that this process would diverge if P_k was larger than $P_{\rm abs}$ because the higher the energy absorbed by dust, the higher the IR heating flux. That implies that the convergence can only be reached from lower values of P_k.

In practice, the incident spectrum at $\lambda \geq 912\,\AA$ is divided into 75 individual wavelengths bands (21 in the VIS-UV between $\lambda_L = 912\,\AA$ and $\lambda_V = 0.55\,\mu m$) with enough points to accurately sample the region around PAH IR features. In particular, this allow to compute properly the role of these features in the heating of the well shielded regions. The radiative transfer calculations are performed on a specific grid of 64 wavelengths in the UV (37 nm to 1.6 μm) and 64 wavelengths in the IR (1.6 μm-2 mm) chosen to sample correctly the features in the absorption cross section of the various types of dust considered. The IR spectra are computed on a grid of 70 wavelengths in the range $0.36\,\mu m < \lambda < 2\,mm$. 30 individual angles in the range $-1 \leq u \leq +1$ are used for integration in Eq. (1). These angles are different for each layer and chosen to minimize the error in the integral of Eq. (1). In particular, more angles are present near $u = u_l$, the direction tangent to the inner layer (see Fig. 1) where the optical depths is rapidly varying. This is less critical for the other inner shells because the fraction of heating energy for layer i coming from the corresponding solid angles is generally much smaller. The same set of angles is used for the ISRF (Eq. (1)) and the IR heating (Eq. (3)) integration. The choice of the number of layers N and their position in the cloud depends on the density structure and is discussed in detail in the next section. We also choose an equal number of lines of sight and layers, with each line of sight pointing toward the center of a layer. Only one or two steps of the IR heating iterative procedure (Eq. 3) are generally sufficient to obtain the convergence, the main effect taken into account being the first step conversion of UV photons in the outer parts of the cloud into VIS-NIR photons that can penetrate deeper in the cloud. In each layer, thermal fluctuations are computed for PAH, VSG and BG with 5, 5 and 10 individual sizes respectively, covering the sizes range affected to each type of particle (DBP). When thermal fluctuations are found to be less than 0.2 K, the emission is computed at thermal equilibrium.

The FORTRAN code was optimized for parallel computers and used at the CRAY-X/MP18 facility at JPL-Caltech. A typical individual run of the grid presented here needed $\simeq$ 3 min computing time for 100 layers and no IR heating calculations.

2.2. *Description of the set of models*

We present results of the previous model for a series of clouds with various total visual extinction A^{c}_{v} toward the cloud center in the range 1-500 mag and a power law gas distribution of the form:

$$n_{\rm H}(r) = \begin{cases} n^{\circ}_{\rm H}\,(r/r_l)^{-\beta} & for\ r_m > r > r_l \\ n^{\circ}_{\rm H} & for\ r < r_l \end{cases} \quad (5)$$

where $n^{\circ}_{\rm H}$ is a constant density in the $0 < r < r_l$ region. In one set of models, the dust composition was fixed throughout the cloud to the one proposed by DBP (see table 2 of DBP). For this homogeneous dust composition, the extinction curve is similar at every position in the cloud and to the average extinction curve of the ISM. In the visible, this correspond to an extinction of $A_v/N_{\rm H} \simeq 5\,mag/(10^{22}\,{\rm H/cm^2})$, so that the total visual extinction through the cloud center is given by:

$$A^{c}_{v}({\rm mag}) = 1\,10^{-21}\,[n^{\circ}_{\rm H}\,r_l + \int_{r_l}^{r_m} n_{\rm H}(r){\rm d}r]\ ({\rm H/cm^2}) \quad (6)$$

The gas density $n^{e}_{\rm H} = n_{\rm H}(r_m)$ at the edge of the cloud is:

$$n^{e}_{\rm H} = n^{\circ}_{\rm H}(r_m/r_l)^{-\beta}, \quad (7)$$

and was set to $n_H^e = 50\,H/cm^3$, a characteristic value for H_I clouds. For the purpose of comparison with other models (see Section 4) which have often been limited to homogeneous cases, we have considered a few homogeneous clouds (case 201 to 205 in Table 1). In that case, the external radius was arbitrarily set to 1 pc.

The set of models covers a large dynamical range of parameters, in order to explore the hierarchical structure of the ISM from large complexes down to dense cores. For a given choice of the parameters A_v^c, n_H^o and β, the radii r_m and r_l are computed using Eq. (6) and Eq. (7) and are proportional to A_v^c. Table 1 shows the different values of the parameters that we have considered. The 3 digit number in column 1 is a code for n_H^o, β and A_v^c (first, second and third digit respectively). From the central case ($n_H^o = 10^4\,H/cm^3$, $\beta = 2$), we have explored independent variations of the central density in the range $10^3 \leq n_H^o \leq 10^5$ for $\beta = 1$ and 2 and a set of low to moderate extinctions (1 mag $\leq A_v^c \leq$ 50 mag). For $\beta = 1$, only the clouds with $r_m < 40\,pc$ were considered which limit A_v^c to 30 mag for $n_H^o = 10^3$ and $10^4\,H/cm^3$. We also examined denser cases with $n_H^o = 10^6\,H/cm^3$ and higher central extinctions (100 mag $\leq A_v^c \leq$ 500 mag).

The incident radiation field on the cloud has been supposed to be the isotropic local ISRF proposed by Mathis et al.(1983) in the UV-NIR portion but include an estimation of the IR flux based on IRAS large scale emission of the galactic plane (Pérault et al. 1989). No photons at $\lambda < 912\,\AA$ were considered in this spectrum.

2.3. *Layer structure*

The layer model described in section 2, approximates the density of Eq. (5) by a discrete number of concentric layers with constant density $\tilde{n}_H(i) = n_H(r(i))$ where $r(i)$ is the radius of the center of the i^{th} layer. We show in the Appendix that this approximation tends to underestimate the heating in the low extinction regions of the cloud when the layer sampling is not adequately chosen and/or if the total number of layers is too small. This can lead to underestimate the IR LB. The effect of the layer sampling on the computed emission profiles is illustrated in Fig. 2 where the IRAS brightness profiles computed for our central case ($\beta = 2$, $n_H^o = 10^4\,H/cm^3$) with $A_v^c = 50$ mag is plotted for different choices of the layer radii. The continuous line is for a layer radii distribution optimized as described in the Appendix (corresponding to $f = 0.127$ in Eq. (10) of the Appendix), the short dashed line represent a slightly different sampling with larger layer thicknesses in the outer part of the cloud ($f = 1.0$). Both runs were performed with the same total number of layers ($N = 100$). The computed brightness profiles in the non optimized case underestimates the LB in the 4 IRAS bands by a factor of about 1.1. As explained in more details in the Appendix, the layer approximation generally underestimates (respectively overestimates) the radiation field in the outer (resp. inner) regions of the cloud. This produces an error on the emergent IR intensity ($\Delta I/I$) estimated in the Appendix which is a function of the number of layers in the model and their distribution in the cloud. For all the calculations presented here, we have chosen $N = 100$ for $A_v^c > 4$ mag and $N = 50$ for $A_v^c = 1$ mag and a layer distribution optimized to minimize the error on the emergent IR intensity ($\Delta I/I$) which is found to be less than 7 % for all the runs presented.

Table 1. Physical parameters for the runs of our grid. Column 1 is a 3 digit code for β the index of the power law distribution (column 2), n_H^o the central density (column 3) and A_v^c the total visible extinction through the cloud (column 4). r_m (column 6) and r_l (column 7) are the radii of the cloud and of the central constant density region respectively. Both r_l and r_m are proportional to A_v^c for at fixed β and n_H^o. The mass in column 8 is the total gas mass of the cloud

code	β	n_H^0 cm^{-3}	A_v^c mag	r_m pc	r_l pc	Mass $M_\odot$
121	2	1[3]	1	8.11[-1]	1.81[-1]	8.28[0]
122			4	3.24[0]	7.24[-1]	5.28[2]
123			6	4.86[0]	1.09[0]	1.78[3]
124			10	8.11[0]	1.81[0]	8.28[3]
125			30	2.43[1]	5.44[0]	2.24[5]
126			50	4.06[1]	9.07[0]	1.04[6]
221	2	1[4]	1	2.36[-1]	1.67[-2]	2.04[-1]
222			4	9.44[-1]	6.68[-2]	1.31[1]
223			6	1.42[0]	1.00[-1]	4.41[1]
224			10	2.36[0]	1.67[-1]	2.04[2]
225			30	7.08[0]	5.01[-1]	5.52[3]
226			50	1.18[1]	8.35[-1]	2.56[4]
321	2	1[5]	1	7.28[-2]	1.63[-3]	5.99[-3]
322			4	2.91[-1]	6.51[-3]	3.83[-1]
323			6	4.37[-1]	9.77[-3]	1.30[0]
324			10	7.28[-1]	1.63[-2]	5.99[0]
325			30	2.19[0]	4.89[-2]	1.62[2]
326			50	3.64[0]	8.14[-2]	7.49[2]
111	1	1[3]	1	1.61[0]	8.06[-2]	3.25[1]
112			4	6.45[0]	3.23[-1]	2.08[3]
113			6	9.67[0]	4.84[-1]	7.02[3]
114			10	1.61[1]	8.06[-1]	3.25[4]
115			30	4.84[1]	2.42[0]	8.79[5]
211	1	1[4]	1	1.02[0]	5.12[-3]	8.31[0]
212			4	4.09[0]	2.05[-2]	5.31[2]
213			6	6.14[0]	3.07[-2]	1.80[3]
214			10	1.02[1]	5.12[-2]	8.31[3]
215			30	3.07[1]	1.53[-1]	2.24[5]
311	1	1[5]	1	7.49[-1]	3.75[-4]	3.26[0]
312			4	3.00[0]	1.50[-3]	2.09[2]
313			6	4.49[0]	2.25[-3]	7.03[2]
314			10	7.49[0]	3.75[-3]	3.26[3]
315			30	2.25[1]	1.12[-2]	8.81[4]
316			50	3.75[1]	1.87[-2]	4.08[5]
201	0	3.22[2]	1	1.00[0]		3.34[1]
202		1.29[3]	4	1.00[0]		1.33[2]
204		3.22[3]	10	1.00[0]		3.34[2]
205		9.66[3]	30	1.00[0]		1.00[3]
427	2	1[6]	100	2.29[0]	1.62[-2]	1.86[2]
428			200	4.57[0]	3.23[-2]	1.48[3]
429			500	1.14[1]	8.08[-2]	2.32[4]

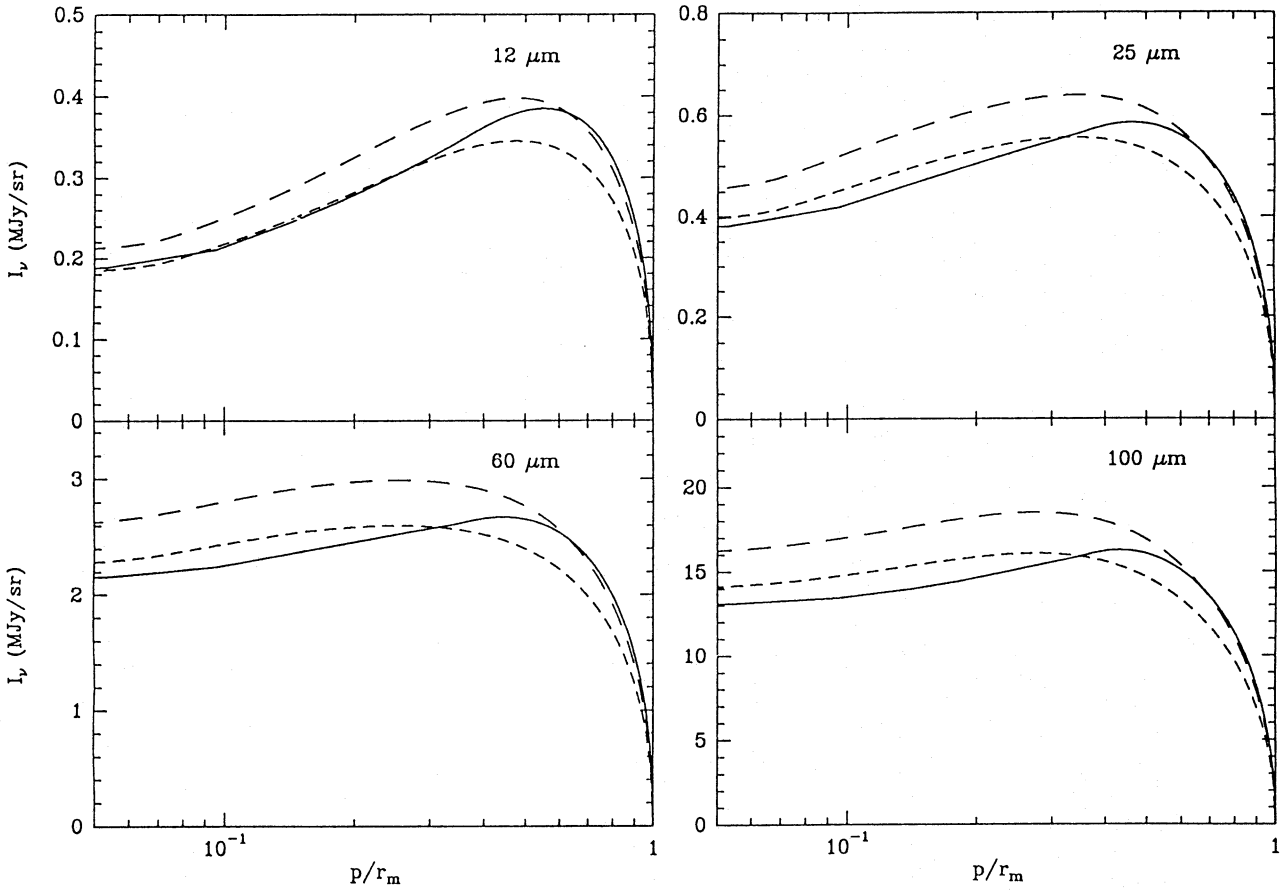

Fig. 2. Surface brightness in the 4 IRAS bands as a function of the impact parameter of the line of sight normalized to the external radius for the central case ($\beta = 2$, $n_H^o = 10^4$ H/cm^3) with a central total extinction $A_v^c = 50$ mag. The solid line is the result for an optimized choice of the layer structure (see text) with $f = 0.127$. The short dashed profile is the prediction for a different (unoptimized) layer distribution ($f = 1$). The long dashed curves is the results of the unoptimized case corrected for the error introduced in the radiative transfer by the model layer using $(\Delta I/I)_{\lambda_L}$ of the Appendix

3. Results

3.1. Global emission and dust temperature

The total emission of the cloud $\mathscr{L}_\nu$ normalized to its mass M_{tot}:

$$\mathscr{L}_\nu = (4\pi/M_{tot}) \int_0^{r_m} \lambda I_\lambda 2\pi p dp \quad (8)$$

is given in Table 2 for a few FIR-submm wavelengths in units of $L_\odot$ per $M_\odot$ of gas in the cloud. At IRAS wavelengths these values were convolved with the responsivity functions of the IRAS photometric bands. In Fig. 3, $\mathscr{L}_\nu$ is plotted as a function of wavelength. The spectra are dominated by the emission of PAH at $\lambda < 15\,\mu$m and by the grey-body like emission from BG at $\lambda > 70\,\mu$m. In between these two wavelengths, the spectra are flat and dominated by emission from VSG. The PAH emission lines can be seen at 3.3, 6.2, 7.7, 8.6 and 11.3 μm. The peak position of the BG emission shifts toward longer wavelengths with increasing central extinction due to the decrease of their equilibrium temperatures.

$\mathscr{L}_\nu$ decreases with increasing A_v^c because the fraction of the dust mass reached by the incident radiation is lower for high than for low extinction clouds in our set of models. This decrease is stronger at shorter wavelengths because dust particles experiencing high enough thermal fluctuations to emit at these wavelengths are excited by energetic photons for which the opacity is higher. Only at Submm wavelengths is the decrease significantly reduced but the scatter of $\mathscr{L}_\nu$ values is still > 70 % at 240 μm and > 35 % at 800 μm for the clouds of Fig. 3 (extinctions in the range 1 to 50 mag).

Column 10 of Table 2 show the equilibrium temperatures for 45 nm BG at the center of the clouds. These temperatures depend only on the central extinction A_v^c and are not repeated for identical extinction clouds in Table 1.

3.2. Dust IR heating

We have investigated the effect of including the IR heating (see Eq. (3)) on the results presented above. The iterative procedure described in Section 3 converges in all cases to better than 0.3 % for 2 iterations. The spectral distribution of the radiation field at the center of the cloud is shown in Fig. 4 with various A_v^c (10, 30 and 50 mag) after 0 (no IR heating) and 2 iterations. The IR heating by other dust grains in the cloud is responsible for an increase of the incident radiation field at $\lambda > 4.5\,\mu$m. PAH features emission is also added to the radiation field. For $A_v^c < 30$ mag, this contribution is small compared to the energy contained at shorter wavelength ($\lambda < 2\,\mu$m) where the absorption cross section of dust ($Q_a \propto \lambda^{-1}$) is higher. Therefore, heating by

Table 2. Integrated emission of the clouds of the grid. The code refer to Table (1). The emission integrated in the IRAS bands (column 2-5) and at specific wavelength (zero width assumed) in the FIR-Submm (column 6-9) are in $4\pi\nu I_\nu$ in $L_\odot$ per solar mass of gas in the cloud. Column 10 is the equilibrium temperature of classical grains at the center of the cloud. Subscript 1 refer to runs for which the IR heating was taken into account

code	12 μm	25 μm	60 μm	100 μm	241 μm	400 μm	800 μm	2 mm	T_{BG} K
121	1.50[-1]	9.27[-2]	1.80[-1]	5.76[-1]	3.33[-2]	7.57[-3]	6.82[-4]	1.75[-5]	
122	9.29[-2]	6.06[-2]	1.17[-1]	3.94[-1]	2.75[-2]	6.67[-3]	6.32[-4]	1.68[-5]	
123	7.39[-2]	4.93[-2]	9.47[-2]	3.25[-1]	2.48[-2]	6.24[-3]	6.05[-4]	1.64[-5]	
124	5.31[-2]	3.65[-2]	7.00[-2]	2.44[-1]	2.10[-2]	5.56[-3]	5.61[-4]	1.57[-5]	
125	2.17[-2]	1.61[-2]	3.05[-2]	1.08[-1]	1.24[-2]	3.82[-3]	4.37[-4]	1.36[-5]	
126	1.34[-2]	1.03[-2]	1.95[-2]	6.78[-2]	9.04[-3]	3.01[-3]	3.71[-4]	1.23[-5]	
221	1.90[-1]	1.16[-1]	2.25[-1]	7.07[-1]	3.90[-2]	8.78[-3]	7.82[-4]	2.00[-5]	1.66[1]
222	1.50[-1]	9.34[-2]	1.80[-1]	5.81[-1]	3.52[-2]	8.18[-3]	7.47[-4]	1.94[-5]	1.45[1]
223	1.31[-1]	8.31[-2]	1.60[-1]	5.23[-1]	3.32[-2]	7.83[-3]	7.27[-4]	1.90[-5]	1.35[1]
224	1.08[-1]	6.93[-2]	1.33[-1]	4.44[-1]	3.03[-2]	7.38[-3]	6.99[-4]	1.86[-5]	1.22[1]
225	5.86[-2]	4.00[-2]	7.65[-2]	2.65[-1]	2.21[-2]	5.86[-3]	6.01[-4]	1.71[-5]	9.12[0]
226	4.03[-2]	2.84[-2]	5.42[-2]	1.90[-1]	1.79[-2]	5.03[-3]	5.41[-4]	1.61[-5]	7.98[0]
321	2.18[-1]	1.31[-1]	2.55[-1]	7.89[-1]	4.18[-2]	9.29[-3]	8.22[-4]	2.08[-5]	
322	1.91[-1]	1.16[-1]	2.25[-1]	7.04[-1]	3.93[-2]	8.90[-3]	7.98[-4]	2.03[-5]	
323	1.78[-1]	1.09[-1]	2.11[-1]	6.66[-1]	3.81[-2]	8.72[-3]	7.87[-4]	2.01[-5]	
324	1.61[-1]	9.95[-2]	1.92[-1]	6.12[-1]	3.64[-2]	8.43[-3]	7.71[-4]	2.00[-5]	
325	1.12[-1]	7.18[-2]	1.38[-1]	4.57[-1]	3.09[-2]	7.51[-3]	7.14[-4]	1.91[-5]	
326	8.73[-2]	5.74[-2]	1.10[-1]	3.72[-1]	2.74[-2]	6.90[-3]	6.74[-4]	1.85[-5]	
111	1.82[-1]	1.12[-1]	2.17[-1]	6.93[-1]	3.95[-2]	8.98[-3]	8.04[-4]	2.06[-5]	
112	1.14[-1]	7.41[-2]	1.43[-1]	4.83[-1]	3.32[-2]	8.02[-3]	7.52[-4]	1.99[-5]	
113	8.95[-2]	6.00[-2]	1.15[-1]	3.99[-1]	3.03[-2]	7.54[-3]	7.27[-4]	1.96[-5]	
114	6.22[-2]	4.33[-2]	8.26[-2]	2.92[-1]	2.57[-2]	6.77[-3]	6.79[-4]	1.89[-5]	
115	2.36[-2]	1.80[-2]	3.38[-2]	1.19[-1]	1.52[-2]	4.73[-3]	5.42[-4]	1.67[-5]	
211	1.96[-1]	1.20[-1]	2.32[-1]	7.31[-1]	4.03[-2]	9.11[-3]	8.12[-4]	2.07[-5]	
212	1.47[-1]	9.38[-2]	1.81[-1]	6.00[-1]	3.85[-2]	9.08[-3]	8.39[-4]	2.19[-5]	
213	1.16[-1]	7.61[-2]	1.46[-1]	4.97[-1]	3.47[-2]	8.40[-3]	7.88[-4]	2.09[-5]	
214	8.36[-2]	5.68[-2]	1.08[-1]	3.81[-1]	3.04[-2]	7.71[-3]	7.49[-4]	2.03[-5]	
215	3.59[-2]	2.61[-2]	4.91[-2]	1.75[-1]	1.84[-2]	5.28[-3]	5.73[-4]	1.71[-5]	
311	2.04[-1]	1.24[-1]	2.40[-1]	7.51[-1]	4.09[-2]	9.19[-3]	8.16[-4]	2.07[-5]	
312	1.49[-1]	9.42[-2]	1.82[-1]	5.95[-1]	3.68[-2]	8.58[-3]	7.85[-4]	2.03[-5]	
313	1.35[-1]	8.63[-2]	1.67[-1]	5.52[-1]	3.55[-2]	8.38[-3]	7.72[-4]	2.01[-5]	
314	1.03[-1]	6.78[-2]	1.31[-1]	4.44[-1]	3.16[-2]	7.75[-3]	7.37[-4]	1.97[-5]	
315	4.74[-2]	3.38[-2]	6.40[-2]	2.28[-1]	2.21[-2]	6.08[-3]	6.31[-4]	1.81[-5]	
316	2.99[-2]	2.19[-2]	4.10[-2]	1.45[-1]	1.60[-2]	4.75[-3]	5.32[-4]	1.64[-5]	
201	1.42[-1]	9.07[-2]	1.76[-1]	5.82[-1]	3.65[-2]	8.52[-3]	7.82[-4]	2.03[-5]	
202	6.27[-2]	4.40[-2]	8.37[-2]	3.00[-1]	2.65[-2]	6.92[-3]	6.88[-4]	1.90[-5]	
204	2.71[-2]	2.05[-2]	3.83[-2]	1.35[-1]	1.70[-2]	5.12[-3]	5.70[-4]	1.70[-5]	
205	8.45[-3]	6.99[-3]	1.31[-2]	4.25[-2]	7.37[-3]	2.80[-3]	3.80[-4]	1.34[-5]	
427	1.10[-1]	7.04[-2]	1.35[-1]	4.48[-1]	3.04[-2]	7.41[-3]	7.05[-4]	1.89[-5]	7.13[0]
427[1]	1.10[-1]	7.04[-2]	1.36[-1]	4.51[-1]	3.06[-2]	7.46[-3]	7.14[-4]	1.93[-5]	7.51[0]
428	7.71[-2]	5.12[-2]	9.83[-2]	3.34[-1]	2.55[-2]	6.46[-3]	6.39[-4]	1.79[-5]	6.50[0]
428[1]	7.71[-2]	5.12[-2]	9.87[-2]	3.37[-1]	2.56[-2]	6.53[-3]	6.53[-4]	1.82[-5]	6.87[0]
429	4.13[-2]	2.89[-2]	5.53[-2]	1.94[-1]	1.76[-2]	4.79[-3]	5.05[-4]	1.53[-5]	5.84[0]
429[1]	4.13[-2]	2.90[-2]	5.55[-2]	1.96[-1]	1.78[-2]	4.90[-3]	5.27[-4]	1.61[-5]	6.18[0]

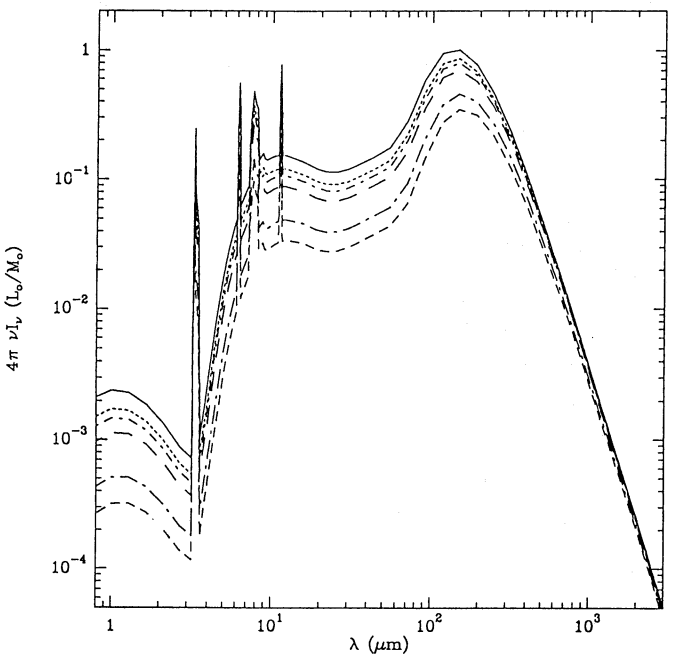

Fig. 3. Global emission spectra for the central case ($\beta = 2$, $n_H^o = 10^4$ H/cm^3) and a total visible extinction toward the center of the cloud (A_v^c) of 1 mag (solid), $A_v^c = 4$ mag (dot), $A_v^c = 6$ mag (dot dash), $A_v^c = 10$ mag (long dash), $A_v^c = 30$ mag (long dot dash), $A_v^c = 50$ mag (short dash). Units are $4\pi\nu I_\nu$ in $L_\odot$ per solar mass of gas in the cloud. The IR features and continuum are due to emission by PAH molecules. FIR-Submm emission is caused by BG which are cooler for denser clouds. The luminosity is progressively proportional to the total mass in the millimetric region. Intermediate wavelength emission is caused by intermediate size VSG

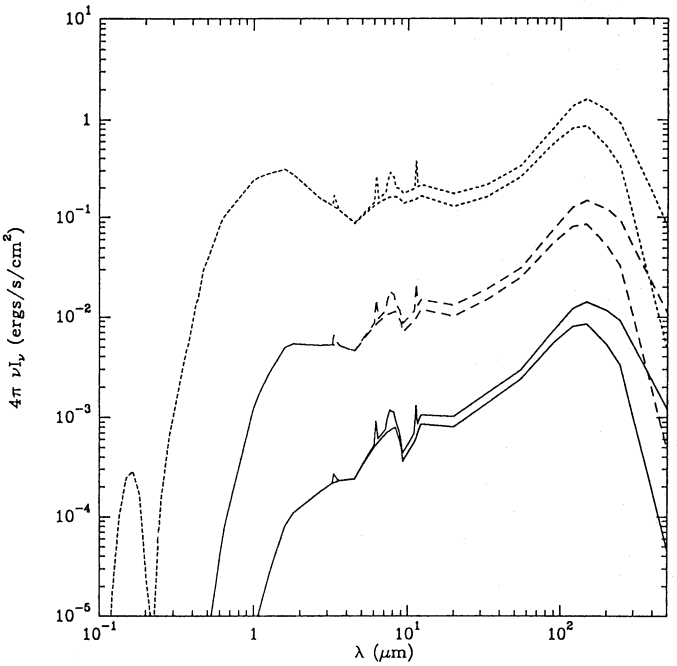

Fig. 4. Incident radiation field at the center of the cloud for the central case with $A_v^c = 50$ (solid), 30 (dash) and 10 mag (dot), with (upper curves) and without (lower curves) IR heating taken into account (2 iterations). The curves for 30 and 10 mag have been multiplied by 10 and 100 respectively

IR radiation from dust in the cloud cannot contribute significantly for $A_v^c < 50$ mag. Table 2 shows the effect of including dust IR heating on the temperature of BG in the cloud center and on the total cloud emission. For $\beta = 2$, $n_H^o = 10^6$ H/cm^3 and $A_v^c = 500$ mag, the IR heating contributes a fractional increase of the BG temperature smaller than 6 % (0.34 K). Because only a small fraction of the cloud mass (inner regions) is affected, the corresponding increase of the submm emission (2 mm) is about 5 %. The emission at IR wavelengths, which is dominated by small particles, is not affected by adding VIS-NIR photons in the radiation field because the low energy of these photons cannot increase the amplitude of small grains thermal fluctuations. One reason for the weakness of the effect is that the solar neighborhood ISRF used in these calculations only has a small fraction of its energy in the UV. We note that this could be different in the vicinity of hot stars. As addition of the IR heating by dust has an effect of the same order of magnitude as the error introduced by the layer approximation, it is not taken into account in the calculations for clouds heated by a standard ISRF presented in the following.

3.3. *IRAS emission*

Figure 5 shows the brightness profiles at IRAS wavelengths for the central case $\beta = 2$, $n_H^o = 10^4$ H/cm^3 as a function of the normalized impact parameter p/r_m. All profiles show the same qualitative behavior: at small extinctions ($A_v^c < 4$ mag), the brightness at the cloud center I_c exhibit an increase proportional to A_v^c. This increase stops for $A_v^c \simeq 4 - 6$ mag around $I_{12} \simeq 0.4$, $I_{25} \simeq 0.6$, $I_{60} \simeq 3$ and $I_{100} \simeq 19$ MJy/sr. The saturation of the maximum surface brightness is accompanied by the appearance of the limb brightening effect in the IRAS wavelength range. The radial position of the brightness maximum progressively moves toward the exterior of the cloud with increasing central extinction. The low amplitudes of the color variations across the cloud shown in Fig. 6 also reflect the similarity of the behavior of the various IRAS profiles with increasing A_v^c. In general, colors of the form $I_\nu(\lambda_1)/I_\nu(\lambda_2)$ with $\lambda_1 < \lambda_2$ decrease toward the center of the cloud. For $A_v^c = 50$ mag, the color variations from the edge to the center are about 57, 31, 12 and 36 % for 12/100, 25/100, 60/100 and 12/25 respectively and are lower for lower extinction clouds. The amplitude of these variations is low because the brightness profiles show a similar behavior in the 4 IRAS bands. The arrow in Fig. 6 indicates the color value of the same dust mixture in the diffuse medium computed by DBP. A difference of 13.5, 8.7, 18 and 3.6 % for the 12/100, 25/100, 60/100 and 12/25 colors, respectively, with our values at the edge of the $A_v^c = 1$ *mag* cloud is due to the partial shade of the ISRF radiation field by the inner regions of the cloud. The characteristics of the IRAS profiles for the other cases we have investigated are generally similar to the one described above. We find a slightly increasing threshold value A_v^c for the appearance of the LB effect with IRAS wavelengths (from 4 mag at 12 μm to $\simeq$ 10 mag at 100 μm for all the $\beta = 2$ cases) and approximately the same maximum value for the surface brightness in each IRAS band. Table 3 shows the values of the IRAS LB defined by:

$$LB_\lambda = \mathrm{Max}(I_{\lambda(p)}/I_{\lambda(p=0)}), \quad (9)$$

the location p_M of the maximum intensity in the cloud, and the central brightness (I_c). It also gives the visible extinction A_v^l, computed radially from the cloud surface, at the location of

Table 3. Structure of the IRAS profiles for the set of clouds. Codes in column 1 refer to Table 1. The impact parameter of the line of sight corresponding to the maximum emission (p_M) normalized to the cloud outer radius, the central brightness (I_c) and the LB (as defined in the text) are given for each IRAS band. Values of p_M and LB have been omitted when $p_M = 0$ (LB=1)

code	$\frac{p_M}{r_m}$	12 μm I_c MJy/sr	LB	$\frac{p_M}{r_m}$	25 μm I_c MJy/sr	LB	$\frac{p_M}{r_m}$	60 μm I_c MJy/sr	LB	$\frac{p_M}{r_m}$	100 μm I_c MJy/sr	LB	12 μm A_v^l mag	100 μm A_v^l mag
121		2.78[-1]			3.74[-1]			1.75[0]			9.73[0]			
122	2.01[-1]	3.82[-1]	1.03		5.92[-1]			2.80[0]			1.73[1]		9.92[-1]	
123	2.28[-1]	3.59[-1]	1.08	1.99[-1]	5.92[-1]	1.03	1.89[-1]	2.83[0]	1.01	1.60[-1]	1.77[1]	1.01	1.27[0]	1.97[0]
124	4.01[-1]	3.07[-1]	1.24	2.81[-1]	5.46[-1]	1.08	2.15[-1]	2.68[0]	1.04	2.15[-1]	1.65[1]	1.04	9.31[-1]	2.27[0]
125	7.69[-1]	1.92[-1]	2.18	7.02[-1]	3.89[-1]	1.60	6.91[-1]	2.06[0]	1.35	6.78[-1]	1.22[1]	1.36	5.64[-1]	8.92[-1]
126	8.70[-1]	1.57[-1]	3.02	8.32[-1]	3.23[-1]	2.16	8.26[-1]	1.80[0]	1.69	8.06[-1]	1.07[1]	1.68	4.67[-1]	7.52[-1]
221		2.82[-1]			3.78[-1]			1.77[0]			9.81[0]		1.12[0]	
222	6.09[-2]	4.08[-1]	1.01		6.25[-1]			2.96[0]			1.81[1]		1.37[0]	
223	7.32[-2]	3.91[-1]	1.05	5.80[-2]	6.34[-1]	1.01		3.04[0]			1.88[1]		1.25[0]	2.85[0]
224	1.27[-1]	3.46[-1]	1.15	8.32[-2]	6.04[-1]	1.04	6.01[-2]	2.98[0]	1.02	6.01[-2]	1.82[1]	1.02	9.43[-1]	1.40[0]
225	3.67[-1]	2.24[-1]	1.70	3.02[-1]	4.41[-1]	1.32	2.81[-1]	2.38[0]	1.14	2.81[-1]	1.44[1]	1.15	9.43[-1]	1.40[0]
226	5.55[-1]	1.82[-1]	2.12	4.53[-1]	3.67[-1]	1.59	4.53[-1]	2.12[0]	1.26	4.32[-1]	1.29[1]	1.26	7.31[-1]	1.20[0]
321		2.86[-1]			3.82[-1]			1.79[0]			9.91[0]			
322	1.89[-2]	4.16[-1]	1.01		6.36[-1]			3.02[0]			1.84[1]		1.17[0]	
323	2.15[-2]	4.04[-1]	1.04	1.81[-2]	6.51[-1]	1.01		3.13[0]			1.92[1]		1.53[0]	
324	4.20[-2]	3.62[-1]	1.13	2.36[-2]	6.24[-1]	1.04	2.08[-2]	3.09[0]	1.01	2.08[-2]	1.87[1]	1.01	1.28[0]	2.64[0]
325	1.21[-1]	2.57[-1]	1.54	8.19[-2]	5.01[-1]	1.24	5.85[-2]	2.73[0]	1.08	6.63[-2]	1.65[1]	1.09	1.22[0]	2.37[0]
326	1.89[-1]	2.17[-1]	1.79	1.31[-1]	4.39[-1]	1.40	1.02[-1]	2.58[0]	1.13	1.12[-1]	1.59[1]	1.12	1.20[0]	2.22[0]
111		2.90[-1]			3.87[-1]			1.81[0]			1.00[1]			
112		3.88[-1]			6.00[-1]			2.85[0]			1.76[1]			
113	2.49[-1]	3.57[-1]	1.02		5.89[-1]			2.83[0]			1.77[1]		1.04[0]	
114	6.05[-1]	2.87[-1]	1.30	4.70[-1]	5.09[-1]	1.09	4.49[-1]	2.50[0]	1.02	3.94[-1]	1.54[1]	1.02	6.25[-1]	1.16[0]
115	8.89[-1]	1.84[-1]	2.64	8.54[-1]	3.71[-1]	1.91	8.46[-1]	1.93[0]	1.61	8.20[-1]	1.16[1]	1.58	4.39[-1]	7.4[-1]
211		3.01[-1]			4.01[-1]			1.88[0]			1.03[1]			
212		4.01[-1]			6.15[-1]			2.93[0]			1.79[1]			
213		4.01[-1]			6.55[-1]			3.16[0]			1.97[1]			
214	1.12[-1]	3.43[-1]	1.06		6.14[-1]			3.04[0]			1.92[1]		1.73[0]	
215	8.20[-1]	2.06[-1]	2.07	7.55[-1]	3.80[-1]	1.65	7.48[-1]	1.90[0]	1.47	7.01[-1]	1.14[1]	1.47	4.68[-1]	8.39[-1]
311		3.07[-1]			4.08[-1]			1.91[0]			1.05[1]			
312		4.69[-1]			7.15[-1]			3.40[0]			2.07[1]			
313		3.98[-1]			6.16[-1]			2.94[0]			1.80[1]			
314	3.50[-1]	3.08[-1]	1.08		4.97[-1]			2.38[0]			1.47[1]		6.07[-1]	
315	7.24[-1]	2.40[-1]	1.64	6.16[-1]	4.43[-1]	1.32	5.86[-1]	2.22[0]	1.19	5.11[-1]	1.36[1]	1.20	5.58[-1]	1.16[0]
316	8.56[-1]	1.87[-1]	2.42	8.13[-1]	3.46[-1]	1.91	8.02[-1]	1.74[0]	1.69	7.77[-1]	1.04[1]	1.67	4.48[-1]	7.27[-1]
201		2.63[-1]			3.56[-1]			1.66[0]			9.35[0]			
202	7.82[-1]	3.23[-1]	1.21	7.16[-1]	5.12[-1]	1.10	6.90[-1]	2.39[0]	1.07	6.22[-1]	1.51[1]	1.03	4.24[-1]	7.52[-1]
204	9.23[-1]	2.41[-1]	2.19	9.03[-1]	4.35[-1]	1.76	9.00[-1]	2.06[0]	1.61	8.83[-1]	1.25[1]	1.54	3.82[-1]	5.81[-1]
205	9.76[-1]	1.63[-1]	5.14	9.70[-1]	3.16[-1]	3.88	9.68[-1]	1.55[0]	3.32	9.64[-1]	8.34[0]	3.36	3.57[-1]	0.00[0]
427	1.25[-1]	2.04[-1]	1.94	8.45[-2]	3.83[-1]	1.62	6.76[-2]	2.43[0]	1.21	7.62[-2]	1.53[1]	1.16	1.24[0]	2.15[0]
427[1]	1.25[-1]	2.04[-1]	1.94	8.45[-2]	3.83[-1]	1.62	6.76[-2]	2.44[0]	1.21	7.62[-2]	1.57[1]	1.16		
428	2.42[-1]	1.84[-1]	2.09	1.78[-1]	3.16[-1]	1.90	1.48[-1]	2.09[0]	1.36	1.64[-1]	1.37[1]	1.26	1.10[0]	1.79[0]
428[1]	2.42[-1]	1.84[-1]	2.09	1.78[-1]	3.16[-1]	1.90	1.48[-1]	2.10[0]	1.36	1.64[-1]	1.40[1]	1.25		
429	5.28[-1]	1.59[-1]	2.43	4.20[-1]	2.45[-1]	2.41	4.01[-1]	1.50[0]	1.80	4.01[-1]	1.06[1]	1.56	7.90[-1]	1.32[0]
429[1]	5.28[-1]	1.59[-1]	2.43	4.20[-1]	2.45[-1]	2.41	4.01[-1]	1.51[0]	1.80	4.01[-1]	1.07[1]	1.56		

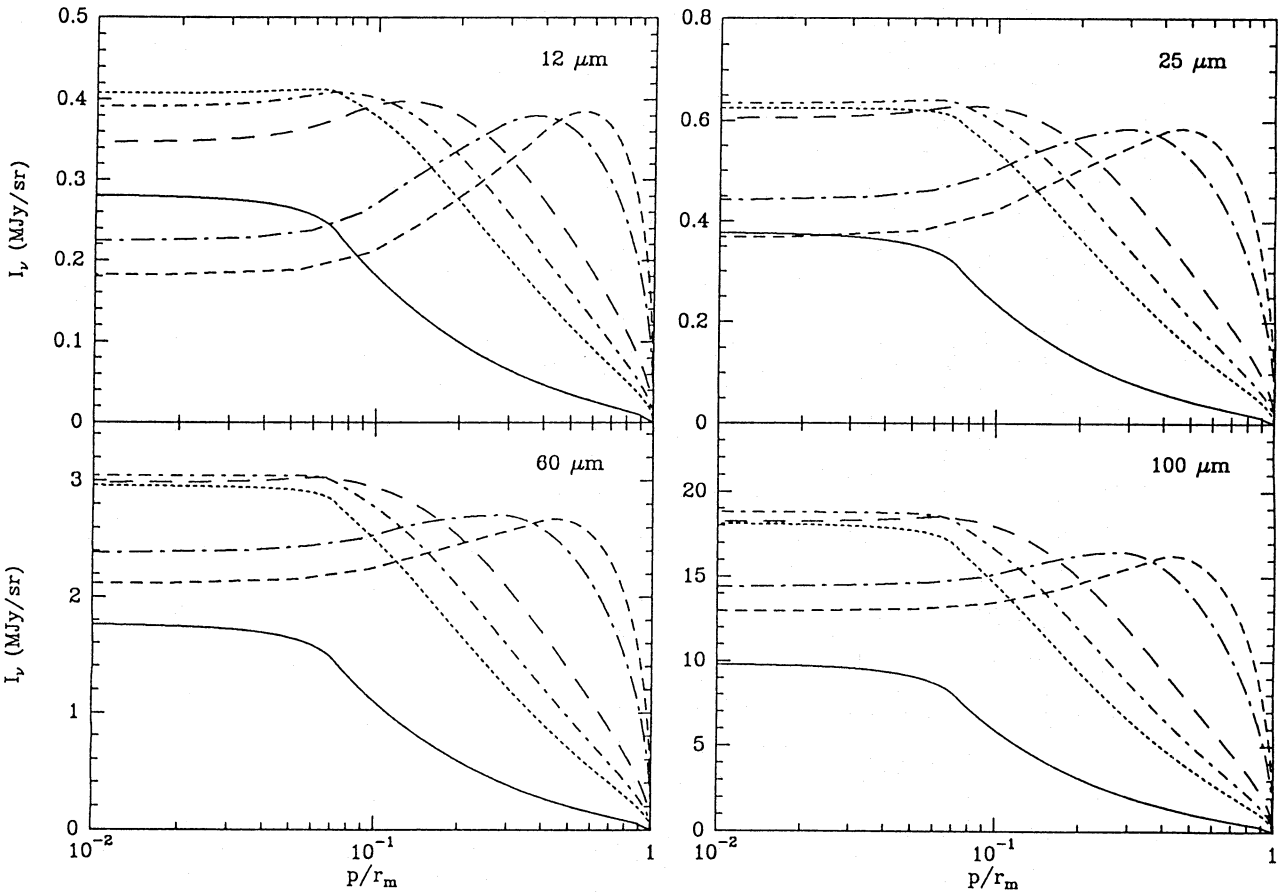

Fig. 5. IR brightness profiles in the 4 IRAS bands for our central case ($\beta = 2$, $n_H^o = 10^4$ H/cm^3). The line codes for the various extinctions are the same than for Fig. 3

maximum brightness ($r = p_M$) for 12 and 100 μm. The LB effect is seen to be sytematically higher for smaller β values.

Figure 7 shows the IRAS profiles obtained for various central extinctions for the homogeneous case. The IRAS LB appears almost simultaneously in the 4 IRAS bands and is higher, for a given extinction, than for inhomogeneous distributions. The position of the maximum intensity is also much closer to the edge of the cloud and the width of the limb region is reduced to a small (< 20 %) fraction of the cloud radius. Unlike for $\beta \neq 0$, where the emission profile depends on the geometry of the cloud (r_m and r_l), the profiles here are independent of the value of r_m. Both the increase of LB and the high values of p_M are due to the density discontinuity near the edge of the cloud and to the fact that photons encounter higher density sooner when penetrating into the cloud.

4. Discussion

4.1. General results

At the edge of a very dense homogeneous cloud ($\beta = 0$), the intensity of the radiation field is decreased by a factor of 2 relative to the diffuse ISM medium situation because of the complete shielding by the cloud over a 2π steradian solid angle. DBP have shown that, for such a decrease of the ISRF (compare result for X=1, table 4 and X=0.5 table 5 in DBP), I_{60} and I_{100} decrease more than I_{12} or I_{25} (which are approximately proportional to X). This is due to the decrease of the temperature of BG with the intensity of the ISRF. Thus, one would expect the 12/100 and 25/100 colors at the edge of such a cloud higher than in the diffuse ISM by almost a factor of 1.25. Our results show that, a more detailed calculation for the radiative transfer and a more realistic density distribution in the cloud ($\beta \neq 0$) does not produce such an increase of these colors near the edge. This is because, for a realistic case, a significant fraction of the solid angle is opaque only to UV photons responsible for the heating of small particles and not to VIS-NIR photons. Only the central core of the cloud, which represent a small fraction of the solid angle at the edge of the cloud, is opaque to all wavelengths radiation so that the decrease of the ISRF is less than a factor of 2 and is not wavelength independent (as the use of the parameter X implies). We have checked that, for flatter distributions and high extinction clouds, the increase of those colors at the edge of the clouds is predicted by our model.

4.1.1. IRAS brightness distribution

As emphasized in Section 3, the shape of the IRAS profiles is sensitive to the mass distribution of the cloud. For instance, the LB values are systematically higher for lower values of β. It is therefore important to constrain the abundance to a realistic value at the edge of the cloud because the distribution of the IR radiation for a non-homogeneous cloud is sensitive to that parameter. For small β, high density regions are close to the cloud surface where

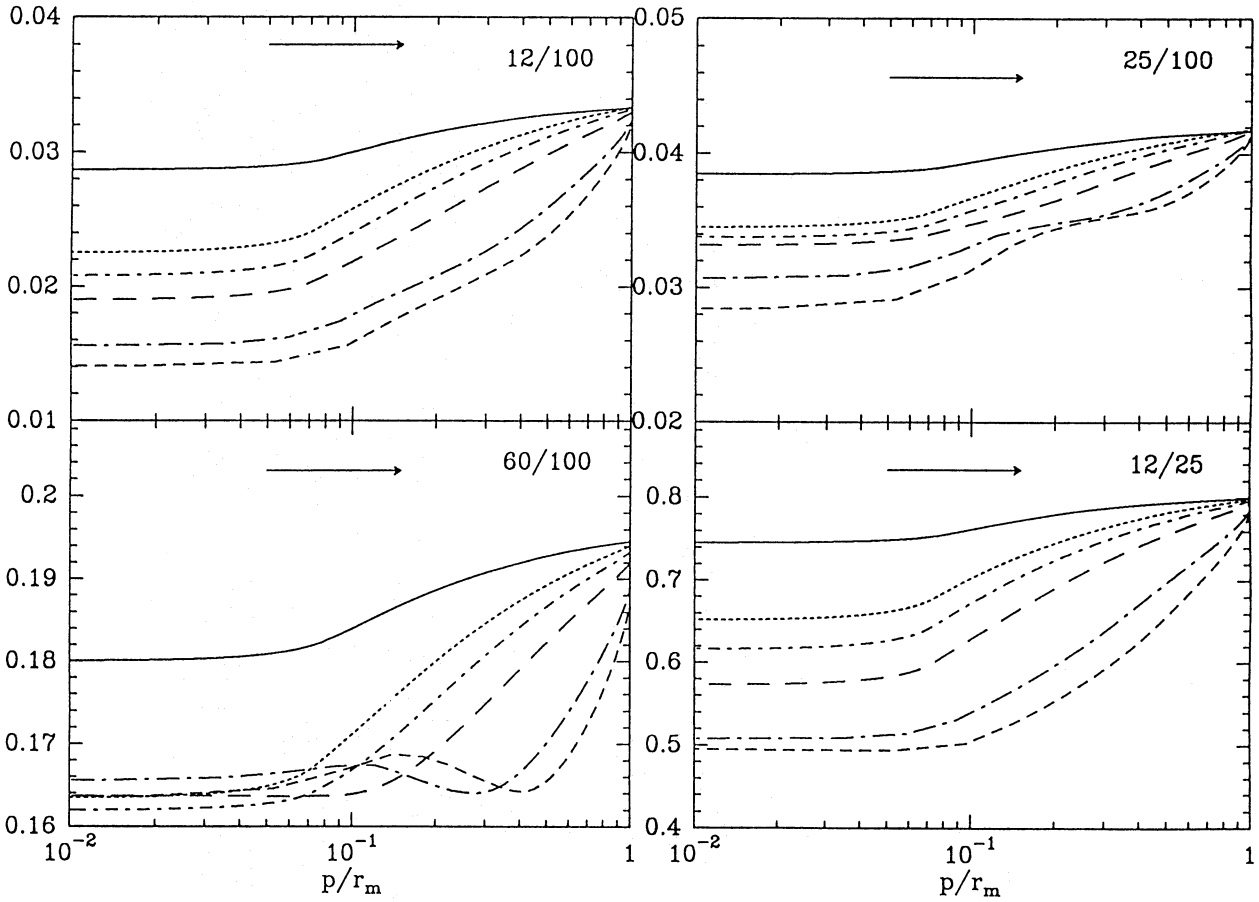

Fig. 6. 12/100, 25/100, 60/100 and 12/25 IRAS color profiles for the central case corresponding to Fig. 3. The line codes for the various extinctions are the same than for Fig. 3. The arrow represents the color expected for the same dust composition heated by the same local ISRF incident radiation but in the diffuse ISM (DBP table 3) where no radiative transfer and projection effect are taken into account. The difference between these values and the color at the edge of the cloud is due to partial shade effect by the opaque parts of the cloud

they are exposed to higher UV flux. As a result, the ISRF is absorbed in a thin shell around the cloud which therefore exhibit a high IR brightness. The extinction of this shell, measured by A_v^l, is small (less than 3 mag) independent of the density structure and slowly decreases for a given density profile, with increasing A_v^c. A striking aspect of the results presented in the previous section is the similarity of IR profiles in all IRAS bands. The 12 and 25 μm LB can be understood as due to the selective extinction of UV photons causing thermal fluctuation in small dust grains. The individual spectra for various line of sight parameters p inside the cloud are shown in Fig. 8 for the case 226. It can be seen on this figure that the emission maximum progressively shifts toward long wavelengths for decreasing impact parameters. This is due to the decrease of the BG equilibrium temperature from the edge to the center of the cloud which provokes the progressive shift of the emission to wavelengths longer than 100 μm. It must be noticed here that the long wavelength cutoff of the 100 μm IRAS band is smaller than the BG peak emission even under ISRF excitation conditions. The 100 μm limb brightening in Fig. 5 is caused partly by this temperature effect, which is dominant at low dust temperatures and by the emissivity loss associated to the progressive decrease of the radiation field into the cloud. The emission in the 20-60 μm region shows a similar thermal effect: the slope of this part of the spectrum increases when penetrating into the cloud. The resulting increase of VSG emission at 100 μm is too small, however to compensate for the effect of the BG cooling on the IR emission in the 100 μm band.

However, the precise location of the maximum brightness in each IRAS band shows a systematic shift toward the outside of the cloud at shorter wavelengths. This disposition of the maximum brightness as a function of λ_{iras} is a consequence of the radiative transfer: the UV photons of the ISRF which are the most efficient in heating smaller grains are present only in outer regions while BG can be heated by VIS-NIR photons which penetrate deeper in the cloud.

An additional consequence of the model presented here is that, although BG which dominate the 100 μm emission are not predominantly heated by UV photons, the I_{100} surface brightness is predicted to show a LB appearing at central extinction through the cloud as low as $\simeq$ 10 mag. The predicted 100 μm LB has not been reported to be seen in IRAS data but could, a priori, be evidenced using correlation studies of the IR emission and an independent column density determination in isolated clouds with $A_v^c > 10$ mag and no strong internal heating sources. However, the determination of the extinction for such clouds is generally difficult due to the small number of stars available for star counts and the 100 μm LB could be smaller than brightness fluctuations in the cloud envelope which account for most of the 100 μm emission.

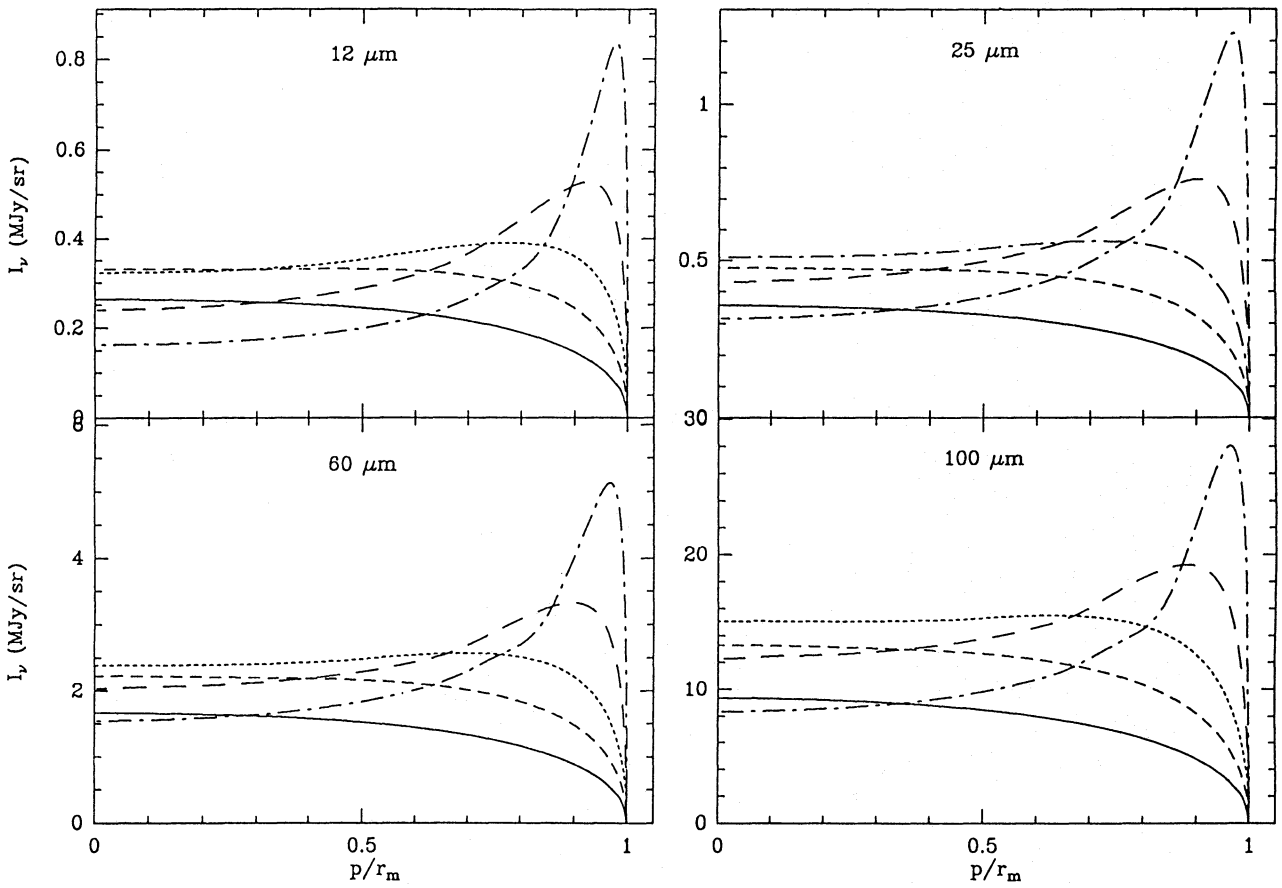

Fig. 7. IRAS profiles for the homogeneous case ($\beta = 0$). The code for the lines is the same that for Fig. 3. The case $A_v^c = 2$ mag (small dashed line) was added for comparison with other models (see text)

4.1.2. Column density determination

A consequence of the 100 μm LB is that, like for shorter IRAS bands, the 100 μm surface brightness cannot be used as a tracer of the column density of dust for $N_H > 10^{22}$ H/cm^2 ($A_v > 5$ mag) because the relationship with $I_{100} - N_H$ is no longer unique. Fig. 9 shows I_{100}/N_H versus N_H for our central case and various central extinctions. For $N_H < 10^{22}$ H/cm^2 where no 100 μm LB happens, I_{100} is seen to be nearly proportional to N_H only toward the outside of each cloud with an I_{100}/N_H value decreasing with increasing A_v^c. This constant value is smaller than the I_{100}/N_H ratio of 85 MJy/sr/10^{22} H/cm^2 derived by Boulanger & Pérault (1988) for atomic gas at high galactic latitude. This difference in outer regions is due to the shielding by the nearby dense regions of the cloud in our case. For $N_H > 10^{21}$ H/cm^2 ($A_v^c > 0.5$ mag), I_{100}/N_H is no longer constant but can still be used to determine N_H. In this region, the curves shown on Fig. 9 have an inflection point and can be approximated by the line drawn in Fig. 9:

$$I_{100} = N_H(-41.20 \log_{10}(N_H) + 923.8) \quad (10)$$

with N_H in H/cm^2 and I_{100} in MJy/sr. This relation is not strongly affected by variations of β or n_H^o in the range investigated and can therefore a priori be used as a column density estimator for projected extinction in the range 1.5-5 mag. However, for real clouds, the shell emitting most of the 100 μm is likely to contain small scale density inhomogeneities that can be misinterpreted as stronger inhomogeneities closer to the cloud center when using Eq. (10) directly. Figure 10 shows the emissivity of the dust for various wavelengths and normalized to its value at the edge of the cloud ($r = r_m$) plotted as a function of the extinction for the case 226 ($A_v^c = 50$ mag). The density contrast of two inhomogeneities producing the same variation of the surface brightness at the edge of the cloud ($\Delta n_H^e/n_H^e$) and at a given extinction A_v ($\Delta n_H/n_H$) are related by $(\Delta n_H/n_H) = (\epsilon_\lambda^e/\epsilon_\lambda(A_v))(\Delta n_H^e/n_H^e)$ where ϵ_λ is the emissivity per unit volume. Figure 10 shows that at $\lambda = 100\mu$m, a density fluctuation near the edge of the cloud can be interpreted as a fluctuation 100 times denser at $A_v = 5$ mag. This figure also shows that only for $\lambda > 200\,\mu$m can $(\Delta n_H/n_H)$ be larger than $(\Delta n_H^e/n_H^e)$ while for $\lambda < 200\,\mu$m, the relative intensity of a density fluctuation giving rise to a given brightness variation is always larger in inner than outer regions. At long enough wavelengths ($\lambda > 240\,\mu$m in that case), $\epsilon_\lambda(A_v)/\epsilon_\lambda^e$ is always larger than 1 so that $(\Delta n_H/n_H) < (\Delta n_H^e/n_H^e)$. When λ increases further, the column density estimation becomes better and better up to the (unreached) limit where $(\epsilon_\lambda(A_v)/\epsilon_\lambda^e) = n_H/n_H^e$ ($\Delta n_H = \Delta n_H^e$).

For extinctions smaller than $\simeq$ 1.5 mag, I_{100}/N_H shows a larger dispersion: I_{100}/N_H increases with decreasing central densities in the cloud. This can be understood because for clouds with a highly centrally peaked mass distribution, most of the extinction responsible for the attenuation of the radiation field at the edge of the cloud is due to the core which fills only a small fraction of the solid angle, so that the emission near the edge is less sensitive to the total cloud extinction. Although observations of

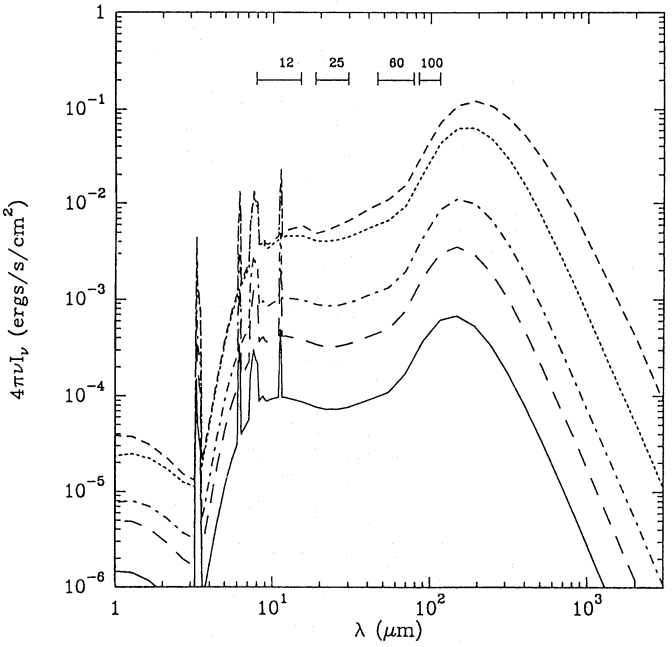

Fig. 8. Individual spectra ($4\pi\nu I_\nu$) versus wavelength for the central case and $A_v^c = 50$ mag at several lines of sight with impact parameter $p/r_m =$ 0 (solid), 0.3 (long dash), 0.55 (dot dash), 0.8 (dot) and 1 (small dashed line). Those spectra are multiplied by 1, 0.5, 1, 5 and 10 respectively

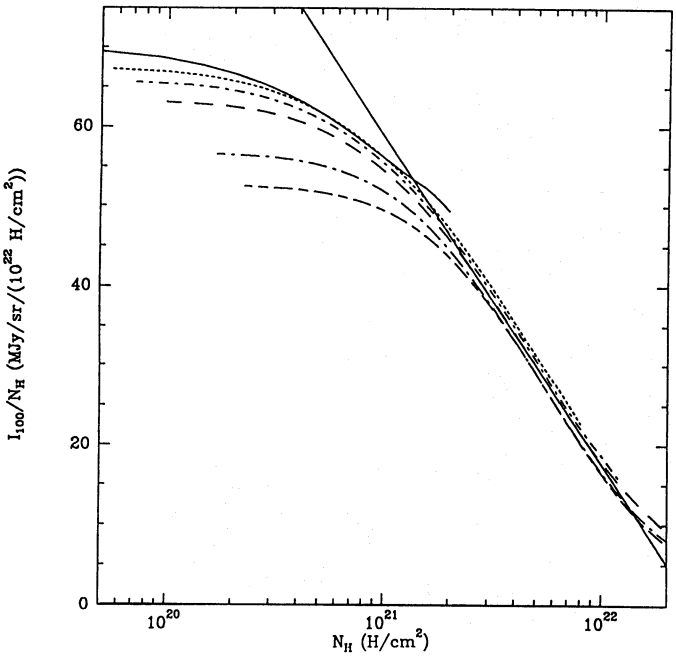

Fig. 9. I_{100}/n_H across clouds of the central case (Fig. 3). Line codes are the same than in Fig. 3. The solid line represent the relation of Eq. (10)

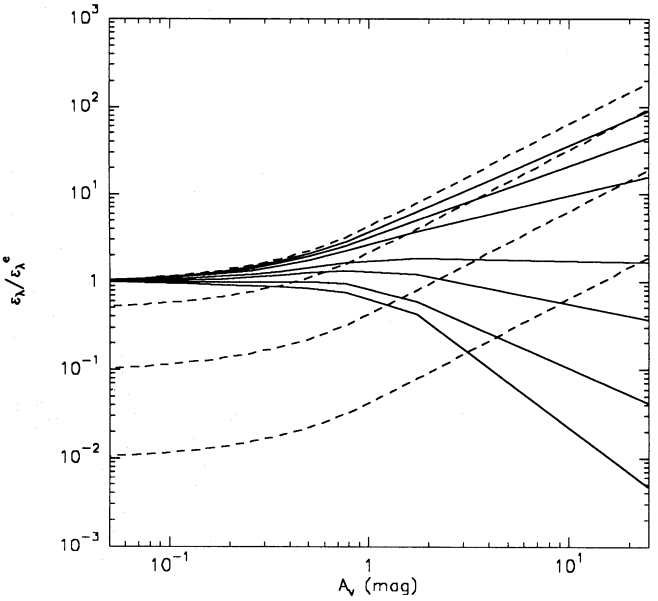

Fig. 10. Emissivity of dust per unit volume (solid lines) normalized to its value in the outer regions of the cloud for the case 226 ($A_v^c = 50\,mag$, $\beta = 2$, $n_H^o = 10^4$ H/cm^3) at various wavelengths: 12, 116, 148, 245, 403, 854 and 2 10^4 μm from the lower to the upper curve. The normalized gas density (n_H/n_H^c) is given by the upper dashed line. The lower dashed lines represent 1/2, 1/10 and 1/100 of this quantity

the 100 μm LB has not been reported, IRAS data shows that the 100 μm surface brightness in isolated clouds is generally smaller than 20 MJy/sr as predicted by our model (Fig. 5). An example is the cloud L134 that exhibits a maximum I_{100} of $\simeq 20\,MJy/sr$ for an extinction $A_B = 10.3$ mag (Laureijs et al. 1991) , 4 times less than expected from I_{100}/A_B relations determined from statistical studies of lower extinction clouds. ($I_{100}/A_v = 8.1$ MJy/sr/mag for the G299-16 cloud: LCCW). This shows that linear correlations cannot be extended to arbitrarily high extinctions. The same effect was reported for the B5 cloud by Langer et al. (1989). Considering a ratio dA_v/dN_H of 5 10^{-22} mag/(H/cm^2) consistent with Eq. (6), the ratio I_{100}/N_H decreases from 38 MJy/sr/(10^{22} H/cm^2) in regions with $0.5 < A_v^c < 1$ to 9 MJy/sr/(10^{22} H/cm^2) at higher extinction in the cloud ($2 < A_v^c < 5$) which is in agreement with results of the Fig. 9. For clouds in the Chamaeleon complex, Boulanger et al. (1992) have shown that I_{100} saturates with increasing column density with a shape of the I_{100}/N_H in good agreement with predictions of this model.

Finally, the results presented in Section 3 have implications on the origin of the heating of dust in strongly obscured regions of molecular clouds. We have seen that even for clouds with total extinctions as high as 500 mag, the temperature of BG near the cloud center is still $\simeq 6$ K. For such high extinctions, the BG temperature is maintained via heating by IR photons at $\lambda \geq 4\mu$m (see Fig. 4). The main source of IR heating in that case appears not to be the IR re-emitted by dust in the cloud but IR photons of the external ISRF itself. This underlines the importance of including the contribution of galactic dust to the IR part of the ISRF. However, this last point is valid only for clouds located far from strong IR emission. For instance, the IR emission associated with a star forming region can easily become stronger than the galactic component and dominate the heating of inner regions of nearby molecular clouds.

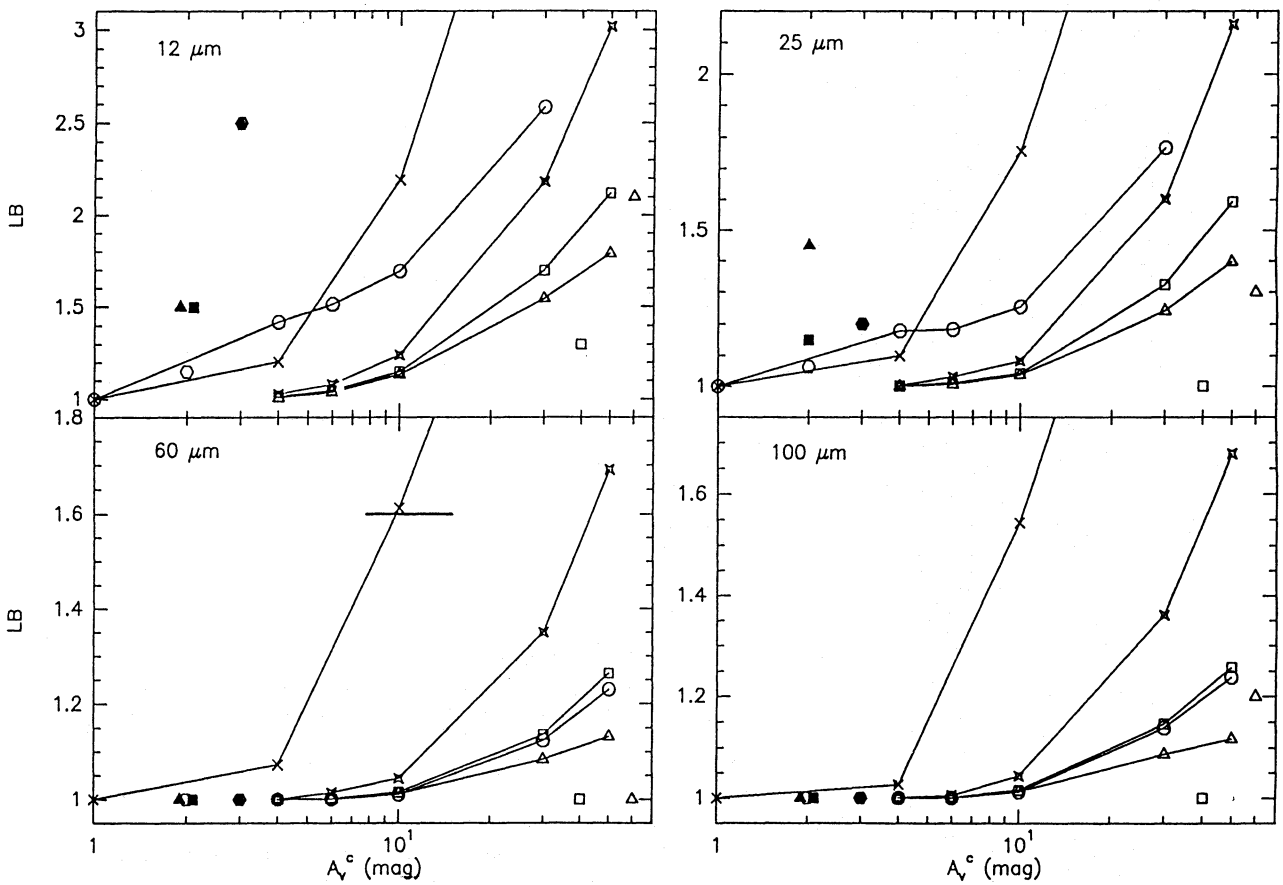

Fig. 11. Limb-Brightening effect in the 4 IRAS bands as a function of the central extinction of the cloud. Values computed using the model presented here with the same set of parameters are open symbols connected for the various central extinctions. The calculated points are: central case (squares), $n_H^o = 10^5\,H/cm^3$, $\beta = 2$ (triangles), $n_H^o = 10^3\,H/cm^3$, $\beta = 2$ (stars) and $\beta = 0$ (crosses). Unconnected open symbols are for models by LL (open square and triangle as explained in the text) Filled symbols are values of the LB for real clouds (see text): G299-16 (triangle), B5 (hexagon), L134 (bar at 60 μm)

4.2. Comparison with observations

4.2.1. Models with a fixed dust composition

Figure 11 shows the values of the LB (defined as the maximum over the central brightness) predicted by the model as a function of the central extinction A_v^c in the 4 IRAS bands. These values are compared to the observed LB values for the cloud G299-16 deduced by LCCW using the symmetrized profile and published and values derived from brightness values along a slice through this cloud (Bernard et al. 1991: triangle). We also plotted LB values calculated from data on the West half of cut 2 of Langer et al. (1989) through the B5 cloud. In this last case, a linear baseline calculated on the extreme points of their published slice was removed. The visual extinction of about 3.5 ± 0.5 mag was taken on the same slice in the extinction map of Cernicharo & Bachiller (1984). We also reported on Fig. 11 the large LB value observed at 60 μm by Laureijs et al. (1991) for the denser cloud L134 with $A_v^c > 7.8$ mag.

Comparison with the predictions of the model shows that, even for the large range of density distributions investigated, the IR LB effect produced by radiative transfer alone is never high enough to explain the LB which is observed for clouds with extinctions as low as $A_v^c = 2 - 4$ mag. As one of the characteristics of the observed LB is to affect essentially the short IRAS wavelengths (primarily 12 and 25 μm and 60 μm in some cases), abundance variations of the smallest dust particles is the most likely explanation. Comparison of the color profiles of Fig. 6 with observed profiles for real clouds leads to a similar conclusion. The colors computed for a constant dust abundance throughout the cloud steadily decrease from the edge to the center of the cloud, while the observed profiles often show 12/100 or 25/100 colors increasing first when penetrating into the cloud and reaching values larger than the diffuse values before decreasing toward the center. This give rise to observed color amplitude variations higher than predicted in Fig. 6. We therefore conclude that abundance variations across the cloud of the particles dominating the IR emission at these wavelengths is more likely responsible for the observed variations.

4.2.2. Models with abundance variations

We have investigated the possibility that the outer regions of the clouds showing the LB effect present an excess of small dust particles compared to the inner regions of the cloud. We modeled this situation by removing PAH particles in the center of the clouds of our central case and increasing the abundance in a 0.5 mag halo around the cloud. The PAH abundance in the halo is chosen in order to produce a maximum surface brightness

Table 4. Same as Table 2 for model similar to the central case but with no PAH (subscript n) and PAH halo as described in the text (subscript h). Run $429^{1,h}$ is similar to run 429^{1} of Table 2 with a PAH halo

code	12 μm	25 μm	60 μm	100 μm	241 μm	400 μm	800 μm	2 mm	T_{BG}
221^{h}	6.55[-1]	2.56[-1]	2.18[-1]	6.59[-1]	3.77[-2]	8.60[-3]	7.86[-4]	2.12[-5]	1.62[1]
222^{h}	4.73[-1]	1.93[-1]	1.67[-1]	5.25[-1]	3.35[-2]	7.92[-3]	7.45[-4]	2.04[-5]	1.45[1]
223^{h}	3.97[-1]	1.65[-1]	1.45[-1]	4.65[-1]	3.14[-2]	7.59[-3]	7.23[-4]	2.00[-5]	1.36[1]
224^{h}	3.06[-1]	1.32[-1]	1.18[-1]	3.87[-1]	2.85[-2]	7.11[-3]	6.91[-4]	1.94[-5]	1.23[1]
225^{h}	1.45[-1]	6.76[-2]	6.54[-2]	2.26[-1]	2.07[-2]	5.67[-3]	5.95[-4]	1.75[-5]	9.13[0]
226^{h}	9.35[-2]	4.52[-2]	4.63[-2]	1.62[-1]	1.68[-2]	4.86[-3]	5.36[-4]	1.63[-5]	7.99[0]
221^{n}	1.14[-2]	6.49[-2]	2.29[-1]	7.27[-1]	3.95[-2]	8.85[-3]	7.85[-4]	1.96[-5]	1.68[1]
222^{n}	9.34[-3]	5.36[-2]	1.88[-1]	6.09[-1]	3.60[-2]	8.30[-3]	7.49[-4]	1.90[-5]	1.48[1]
223^{n}	8.37[-3]	4.83[-2]	1.69[-1]	5.53[-1]	3.41[-2]	8.00[-3]	7.31[-4]	1.87[-5]	1.38[1]
224^{n}	7.04[-3]	4.10[-2]	1.43[-1]	4.76[-1]	3.14[-2]	7.54[-3]	7.04[-4]	1.83[-5]	1.24[1]
225^{n}	4.06[-3]	2.44[-2]	8.45[-2]	2.91[-1]	2.32[-2]	6.05[-3]	6.08[-4]	1.68[-5]	9.14[0]
226^{n}	2.86[-3]	1.76[-2]	6.05[-2]	2.11[-1]	1.89[-2]	5.20[-3]	5.48[-4]	1.58[-5]	7.99[0]
$429^{1,h}$	1.07[-1]	5.09[-2]	4.63[-2]	1.63[-1]	1.65[-2]	4.73[-3]	5.31[-4]	1.68[-5]	6.17[0]

of 0.9-1 MJy/sr at 12 μm. This abundance is in excess to the one inferred for the diffuse ISM by a factor of 4.2 , corresponding to approximately 50 % of the carbon in PAH. These characteristics for the halo approximately match the IRAS observations for the cloud G299-16 in the Chamaeleon complex and may be considered as an extreme case as this cloud shows an unusually high 12 μm surface brightness.

The results for this case (index h) and for a similar case with no PAH in the cloud (index n) are presented in Tables 4 and 5. As PAHs dominate the emission in the IRAS 12 μm band and contribute an important fraction of the 25 μm emission, the case without PAH has a much lower emission in these bands than the central case with a diffuse ISM dust composition (Tables 2 and 3). The halo model shows an increase of 12 and 25 μm emission. As PAHs are responsible for most of the absorption of FUV photons, more of such photons are available to heat VSG and BG in a model with no PAH, so that the associated emission at $\lambda > 60\,\mu$m is increased. At a given wavelength, this increase is limited to less than 8 %. Conversely, for the halo model where PAH are attenuating the UV radiation more efficiently, the emission at $\lambda > 60\,\mu$m is reduced. We also show, in Tables 4 and 5, a case ($429^{1,h}$) similar to the densest cloud of Tables 1 and 2 ($n_{\rm H}^{o} = 10^{6}$ H/cm^{3}, $A_{v}^{c} = 500$ mag) surrounded by a similar halo. We have taken into account the IR heating for this one, in order to investigate possible effect of PAH halo on the heating of dense internal regions of high extinction in MCs. Comparison of the results in Table 4 for this run and results for 429^{1} (Table 2) indicates that the presence of a halo causes almost no change in the temperature of the BG in the cloud center.

We conclude that the effect of PAH halos on the thermal equilibrium of classical grains in the cloud is small and does not affect significantly the FIR-Submm emission of the cloud as long as the incident radiation field does not contain a strong UV component. However, we note that heating of central dense regions by the external PAH halo could play a more important role for clouds heated by a nearby star because the haloes are then brighter.

The result that selective short wavelength LB can be explained by sudden variations of the smallest dust particles abundance in the cloud confirms, on the basis of a complete thermal fluctuation calculations in a self consistent model, the conclusion reached recently by several authors. Boulanger et al. (1990) have evidenced strong large scale variations of the mid-IR to I_{100} ratio in the Chamaeleon, Taurus and Ursa major molecular complexes which they attribute, on the basis of preliminary results of the work presented here, to actual abundance variations of small dust particles. Laureijs et al. (1991) have also concluded that the 60 and 100 μm data in L134, L183 and L1780 can only be interpreted if a specific dust component responsible for the emission at 60 μm encompass a very brutal change of properties in a very narrow transition region. Variations of the abundance of small particles may also imply changes in the optical properties of BG which could affect the Submm-N_H corelation. A more detailed study of some particular clouds (including G299-16) leading to similar conclusions will be presented in a subsequent paper (Bernard et al. 1991).

4.3. Comparison with other models

The results presented in Section 3 can be compared to the predictions of other models for the IR emission of isolated clouds. Mathis et al. 1983 (MMP) have studied the penetration of the ISRF into molecular clouds using the analytical method developed by Flannery et al. (1980) for the radiative transfer calculations. This method, uses spherical harmonics and only considers homogeneous ($\beta = 0$) clouds. Since for large A_{v}^{c}, the equilibrium temperature of the grains at the center of the cloud is independent of both the adopted density distribution and the size of the grains, these quantities can be used to compare the various models. The temperature derived in Table 2 of $\simeq 7.5$ K for BG at the center of a cloud with $A_{v}^{c} = 100$ mag (case 427^{1}) is in good agreement with the temperature derived by these authors of $\simeq 8$ K for graphite grains (their Fig. 6a, $A_{v}^{o} = 50$ mag). The calculations of MMP also included the IR heating by dust. The small difference between these two values can be due to differences in the adopted properties of the grains. In our model we assumed that the BG are composed of a silicate core surrounded by a graphite like mantle having a flat absorption cross section in the UV-VIS. In the MMP model, 0.1 μm silicate grains reach a temperature of almost 6 K under the same conditions.

Table 5. Same as Table 3 for the models of Table 4

code	p_M/r_m	12 μm I_c MJy/sr	LB	p_M/r_m	25 μm I_c MJy/sr	LB	p_M/r_m	60 μm I_c MJy/sr	LB	p_M/r_m	100 μm I_c MJy/sr	LB
221^h		7.78[-1]			7.16[-1]			1.49[0]			8.24[0]	
222^h	1.29[-1]	6.60[-1]	1.42	1.29[-1]	7.63[-1]	1.18		2.60[0]			1.63[1]	
223^h	1.85[-1]	6.07[-1]	1.51	1.85[-1]	7.47[-1]	1.18		2.72[0]			1.72[1]	
224^h	2.72[-1]	5.39[-1]	1.69	2.72[-1]	7.07[-1]	1.25	6.01[-2]	2.67[0]	1.01	6.01[-2]	1.67[1]	1.01
225^h	5.24[-1]	3.65[-1]	2.58	5.24[-1]	5.30[-1]	1.77	2.02[-1]	2.09[0]	1.12	2.29[-1]	1.29[1]	1.14
226^h	6.51[-1]	2.96[-1]	3.34	6.51[-1]	4.39[-1]	2.26	4.08[-1]	1.86[0]	1.23	4.08[-1]	1.15[1]	1.24
221^n		1.87[-2]			2.25[-1]			1.91[0]			1.06[1]	
222^n		3.05[-2]			3.98[-1]			3.40[0]			2.06[1]	
223^n	6.81[-2]	2.99[-2]	1.03	5.80[-2]	4.06[-1]	1.01		3.49[0]			2.14[1]	
224^n	1.05[-1]	2.71[-2]	1.11	6.72[-2]	3.91[-1]	1.04	6.72[-2]	3.41[0]	1.02	6.72[-2]	2.06[1]	1.02
225^n	3.37[-1]	1.76[-2]	1.61	2.81[-1]	2.90[-1]	1.30	2.81[-1]	2.72[0]	1.15	2.81[-1]	1.63[1]	1.15
226^n	4.88[-1]	1.42[-2]	2.00	4.32[-1]	2.42[-1]	1.54	4.32[-1]	2.42[0]	1.27	4.32[-1]	1.47[1]	1.26
$429^{1,h}$	6.24[-1]	3.34[-1]	2.89	4.80[-1]	3.61[-1]	2.84	3.59[-1]	1.24[0]	1.77	3.59[-1]	9.02[0]	1.54

The predictions of MMP of the spectral distribution of the radiation field at various optical depths in an $A_v^c = 400$ mag cloud (their Fig. 4) can be compared to our Fig. 4, although both cases are not strictly equivalent. The radiation field at the center of an $A_v^c = 10$ mag cloud of Fig. 4 show a local maximum in the NIR at $\lambda \simeq 1.5\,\mu$m which is also the approximate wavelength maximum predicted by MMP at a depth of 5 mag in their 400 mag cloud. Absolute values of the incident intensity at this wavelength also compare well if one takes into account the difference of incident ISRF (a factor of 10 at 1.5 μm between a 10 kpc and a 5 kpc distance from the galactic center) and the fact that a 2π sr solid angle is opaque to all radiation at $\lambda = 1.5\,\mu$m in the case investigated by MMP.

Our assumption of completely forward scattering overestimates the radiation field in the cloud compared to models including more realistic scattering properties of dust. The influence of these properties have been studied in detail by Flannery et al. (1980). For values of the single scattering albedo comparable to the one adopted in our model (maximum albedo of BG $\beta_m = 0.6$, see DBP), these authors have shown that the radiation field intensity at a 3 mag depth in an homogeneous cloud varies by a factor of $\simeq 1.3$ from $g = 0.5$ to $g = 0.75$. As observations indicate asymmetry parameters of interstellar dust in the range 0.6-0.9 in the UV (Lillie & Witt 1976), we expect our approximation to produce only a small error in the thin layer ($A_v^1 < 3$ mag) where most of the IR emission occur. The good agreement of our predictions with the results of MPP as far as the incident radiation intensity is concerned support this idea.

Thermal fluctuations of small dust particles in the context of modeling the IR emission of isolated clouds has been considered only by few authors. Lis & Leung 1990 (LL) have recently conducted a study of the IR emission of higher extinction clouds (10 mag $\leq A_v^c \leq$ 2000 mag) with a dust composition including only one size of classical grains (mixture of silicate and graphite grains with $a = 0.1\,\mu$m) and one type of fluctuating graphite grains with size of $10 - 30\,\AA$. They adopted an ISRF spectrum similar to the one considered here and used a transport code allowing calculations for $\beta \neq 0$ (Egan et al. 1988).

As shown above, the IR profiles are generally quite sensitive to the distribution of the mass inside the cloud which is not unique for a given choice of β and r_m but depends on the adopted value for r_1/r_m which is not given in LL. Their results for $\beta = 1$ (their Fig. 6 or table 1) show a LB stronger in the 12 μm band and appearing simultaneously at 12, 25 and 100 μm. The main difference with our model is the value of the central extinction above which the LB effect appears. Their model gives, in the case $\beta = 1$ a threshold value corresponding to $A_v^c \simeq 40$ mag (τ_v=20) higher than our result (see Table 3) of $\simeq$ 10 mag. These values are compared to our result in Fig. 11. In the case $\beta = 0$ they find $LB_{12} \simeq 4.2$ for $A_v^c = 60$ mag while we derive a higher LB of $LB_{12} = 5.25$ for a lower extinction $A_v^c = 30$ mag. Part of the difference can be attributed to the fact that the values quoted by LL are computed using IRAS profiles convolved with a Gaussian beam with a FWHM width of 0.25 pc ($\Delta r/r_m = 0.25$ for their value of $r_m = 1\,pc$) which becomes comparable or larger than the narrow ($\Delta r/r_m < 0.15$) rim present in the unconvolved profiles (Fig. 7). Other possible explanations for the discrepancy between the two models may include differences between the extinction properties assumed in the cloud.

An other important difference between the two models is the spectral distribution of the IR emission. Predictions of a model with only 1 size of small temperature fluctuating particles show a local maximum near 30 μm and a local minimum around 65 μm (see Fig. 2-5 of LL), while the results for a continuous dust size distribution show a smoother spectrum with an approximately flat energy distribution in the range $20 < \lambda < 60\,\mu$m (see Fig. 8). This difference is due to the fact that the amplitude of the temperature fluctuations is size dependent, a size distribution then leading to a smoother spectrum. In the NIR the two models differ notably due to the absence of particles in the LL model small enough to emit at $\lambda < 10\,\mu$m.

Our results are in agreement with the calculations of the $A_v^c = 2$ mag, $\beta = 0$ cloud model developed by Laureijs et al. (1989) (LCCW) to interpret the origin of the IR emission of the cloud G299-16 in the Chamaeleon molecular complex. A dust model was used composed of core-mantle grains, one size of PAH molecules with the IR properties inferred from laboratory results for the coronene molecule and intermediate size grains

composed of small iron particless. The iron particles emit at thermal equilibrium with a high temperature ($T \simeq 50$ K under local ISRF conditions). Their ISRF was similar to the spectrum adopted here and their extinction curve in the cloud also similar to the observed mean extinction curve for the diffuse ISM. Their model lead to a small LB of $\simeq 1.15$ and $\simeq 1.06$ at 12 and 25 μm and no LB at longer wavelengths. These values are also reported in Fig. 11 and are compatible with our results presented in Fig. 7 where the LB at 12 μm appears for $A_v^c > 2$ mag. As noted by LCCW, the 12 μm LB is strongly affected by the UV absorption properties assumed for PAH which could explain the small differences in L_{12} between the two models (we find a $LB > 1$ at 12 and 25 μm only for $2 < A_v^c < 4$ mag see Fig. 7). Our model attributes a fraction of the extinction in the visible to PAHs (see DBP) while no absorption at $\lambda > 2200$ Å is attributed to PAH in the LCCW model.

5. Conclusion

We have used a model for the IR emission and extinction properties of small dust particles proposed recently (DBP) to compute the IR emission in the IRAS photometric bands for a set of isolated, spherical and non-homogeneous clouds heated by the local ISRF, with a total central visual extinction in the range 1-50 mag and a wide range of density structures.

We predict that the IR limb brightening in the IRAS photometric bands caused by selective absorption of UV photons of different energies in the cloud generally happens for central extinctions $A_v^c > 4$ mag at 12 μm, $A_v^c > 10$ mag at 100 μm and intermediate extinctions for the other IRAS bands. The surface brightness in the 4 IRAS bands is limited to $\simeq 0.4$, 0.6, 3 and 19 MJy/sr at 12, 25, 60 and 100 μm respectively as long as no strong density discontinuity is present at the edge of the cloud. We have shown that, even for $A_v^c < 10$ mag where no 100 μm LB occurs, the model predicts a decrease of I_{100}/N_H with N_H that is compatible with the observations. Thus, a non constant ratio must be used when deducing gas column densities from the 100 μm data. This column density indicator is limited to A_v^c smaller than $\simeq 10$ mag due to the 100 μm LB effect.

Finally, the comparison of these results with the observed LB for isolated molecular condensations shows that the actual LB generally exists for clouds with too small an extinction for the effect to be attributed to radiative transfer effects only. As, in addition, the observed LB affects preferentially the short IRAS wavelength emission, we propose that it must be caused by systematic spatial variations of the abundance of the small dust particles in the cloud. In this picture, the limb brightening is caused by an increase of the small dust particles in a halo surrounding the cloud. We showed that such a halo with a PAH abundance increased by a factor of $\simeq 4$ relative to the diffuse ISM standard abundances produces a significant LB at 12 and 25 μm for clouds with extinctions as low as $A_v^c = 4$ mag. We also investigated the effect of such a halo on the global energetics of the cloud and found it to be negligible in all the cases studied.

Acknowledgements. One of us (J.P. Bernard) acknowledges the hospitality of the Caltech University and the Jet Propulsion Laboratory for support during most of this work. It is our pleasure to thank M. Giard for interesting comments and R. Laureijs for constructive discussions and a careful reading of the manuscript.

Appendix

In this Appendix, we show that the approximation of a power law density of the type:

$$n_H(r) = \begin{cases} n_H^o\,(r/r_1)^{-\beta} & for\ r_m > r > r_1 \\ n_H^o & for\ r < r_1 \end{cases} \quad (1)$$

by a step function in the frame of a layer model where the density is constant in each layer, generally tends to underestimate the emergent IR intensity on all lines of sight in the cloud. We derive an estimator of the error introduced by the layer structure that we use to optimize the choice of the layer distribution in the cloud. We assume a set of N concentric layers for the spherical cloud. The sampling of these layers is chosen so that $r = r_1$ correspond to the external edge of a given layer. We also suppose that each layer has a total thickness $\Delta r(i)$ and a central radius $r(i)$. The gas (H) density $\tilde{n}_H(i)$ in each layer representing n_H of Eq. (1) is:

$$\tilde{n}_H(i) = n_H(r(i)). \quad (2)$$

For the layer model, the radial optical depth $\tilde{\tau}_i(\lambda)$ and $\tilde{\tau}'_i(\lambda)$ at wavelength λ, from $r(i)$ to the outer and inner boundary of the layer respectively are equal and given by:

$$\tilde{\tau}_i(\lambda) = \tilde{\tau}'_i(\lambda) = \sigma_\lambda^H\, n_H^o\,(r(i)/r_1)^{-\beta}\,\Delta r(i)/2 \quad (3)$$

where σ_λ^H is the wavelength dependent dust cross section per H atom. For the distribution of Eq. (1), the continuous radial optical τ depth between radius r_1 and r_2 is

$$\tau(\lambda) = \sigma_\lambda^H\, n_H^o\, r_1^\beta \int_{r_1}^{r_2} r^{-\beta}\,dr. \quad (4)$$

If τ_i and τ'_i are the radial optical depths for the layer i corresponding to $\tilde{\tau}_i$ and $\tilde{\tau}'_i$, we have, for $\beta \geq 0$, $\beta \neq 1$ and $\Delta r(i) \ll r(i)$,

$$\left(\frac{\tau_i}{\tilde{\tau}_i}\right) = 2\frac{r(i)^\beta}{1-\beta}\,\frac{(r(i)+\Delta r(i)/2)^{1-\beta} - r(i)^{1-\beta}}{\Delta r(i)} \simeq 1 - \beta(\Delta r(i)/2r(i)) + o(\Delta r(i)/2r(i))^2 \leq 1 \quad (5)$$

$$\left(\frac{\tau_i + \tau'_i}{2\tilde{\tau}_i}\right) = \frac{r(i)^\beta}{1-\beta}\,\frac{(r(i)+\Delta r(i)/2)^{1-\beta} - (r(i)-\Delta r(i)/2)^{1-\beta}}{\Delta r(i)} \simeq 1 + \beta(1+\beta)(\Delta r(i)/2r(i))^2 + o(\Delta r(i)/2r(i))^4 \geq 1. \quad (6)$$

The total optical depth due to a layer is then underestimated by the layer model ($2\tilde{\tau}_i \leq \tau_i + \tau'_i$), so that, when a cloud with a density structure of the form of Eq. (1) is approximated by a layer model represented by Eq. (2), the modeled total optical depth at the center of the cloud $\tilde{\tau}_o = \Sigma\tilde{\tau}_i$ is generally lower than the actual continuous optical depth τ_o. This is a second order effect on $\Delta r(i)/r(i)$. On the other hand, the layer model generally overestimates the radial optical depth due to the layer i at the center of the layer i itself ($\tau_i \leq \tilde{\tau}_i$). In the outer parts of a cloud with no internal sources, most of the heating of a layer is coming from the outside and most of the radial extinction is due to the layer i itself, so that the layer model systematically underestimates the radiation field in each layer and then the IR emission on the corresponding line of sight. Both effects imply that the LB predicted by a layer model is generally underestimated.

Assuming that the IR emissivity of a layer i is proportional to the product of $\tilde{n}_H(i)$ and the radiation field in $r(i)$, an estimation of the resulting error on the line of sight with impact parameter $p = r(i)$ can be evaluated assuming a plane parallel geometry for the radiative transfer and a spherical geometry for the projection on the line of sight:

$$(\Delta I/I)_\lambda(p) = \frac{I(p) - \tilde{I}(p)}{I(p)} = 1 - \frac{\sum_i e^{-\tilde{\tau}} \tilde{n}_H(i) L(i)}{\int_{LOS} e^{-\tau} n_H(l) dl} \quad (7)$$

where $I(p)$ and $\tilde{I}(p)$ are the IR brightness at impact parameter p for a continuous and discrete model respectively. The sum is over the layers crossed along a line of sight and $L(i)$ is the length of the line of sight in layer i. The integral is over the abscissa l along a line of sight and

$$\tilde{\tau} = \sum_{j>i} 2\tilde{\tau}_j + \tilde{\tau}_i \quad (8)$$

$$\tau = \sigma_\lambda^H n_H^o r_1^\beta \int_{r(i)}^{r_m} r^{-\beta} dr \quad (9)$$

For the grid of models presented in this paper, the thickness $\Delta r(i)$ of the i^{th} layer from the center was chosen in the outer regions of the cloud to follow a law of the form:

$$\frac{\Delta r(i)}{r_1} \propto \left(\frac{r_m}{r_1}\right)^{\left(\frac{i-n_1}{N-n_1}\right)^f} - \left(\frac{r_m}{r_1}\right)^{\left(\frac{i-n_1-1}{N-n_1}\right)^f} \quad (10)$$

where N is the total number of layers and n_1 is an arbitrary fraction of this number. At the center of the cloud, this distribution was smoothly connected to a region with constant layer thickness which is well adapted to a constant density. We also imposed that $r = r_1$ correspond to the external boundary of a given layer. For different values of the accumulation parameter f, this layer structure either oversample the outer or the inner regions of the cloud. In practise, f is chosen to minimize the maximum value over the line of sight impact parameters p of the estimator $(\Delta I/I)_\lambda(p)$ of the error produced by the density structure approximation and computed at the Lyman limit $\lambda = \lambda_L = 912\,\mathring{A}$:

$$(\Delta I/I)_{\lambda_L} = \mathrm{Max}((\Delta I/I)_{\lambda_L}(p)) \quad (11)$$

The resulting layer structure depends on the total extinction at the cloud center, the low A_v^c clouds having relatively more layers near the center with a layer sampling following the density distribution while higher A_v^c clouds have a layer structure which tend to oversample the outer parts of the cloud where most of the IR emission occurs.

The long dashed line of Fig. 2 is the result for the unoptimized case corrected using $(\Delta I/I)_{\lambda_L}(p)$. The correspondence with the optimized results in the outer regions of the cloud indicate that this quantity is a good estimation of the error introduced by the layer sampling in this region. It also overestimates the error toward inner regions and for the long IRAS wavelengths. For the optimal layer distribution defined previously, we have found that the maximal value of the relative error $(\Delta I/I)_{\lambda_L}$ increases, at a fixed total number of layers in the model, from $A_v^c = 0$ to $A_v^c = 2 - 4$ mag and then converges toward a fixed value at higher A_v^c. This implies that IR emission of high extinction clouds can be modeled with the same number of layers than moderate extinction ones as long as the layer distribution is adjusted to minimize $\Delta I/I$, because most of the IR emission is coming from the outer regions of the cloud. $(\Delta I/I)_\lambda$ also decreases linearly with the total number of layers.

References

Allamandola L.J., Tielens A.G.G.M., Backer J.R., 1985, ApJ (letters) 290, L25

Beichman C.A., Wilson R.W., Langer, W.D., Goldsmith P.F., 1988, ApJ (letters) 332, L81

Bernard J.P., Boulanger F., Desert, X., Puget J.L., 1991, In preparation

Boulanger F., Pérault M., 1988, ApJ 330, 964

Boulanger F., Falgarone E., Helou G., Puget J.L., 1989, Proceedings of the I.A.U. Symposium 135 on the interstellar dust, Eds L.J. Allamandola and A.G.G.M. Tielens, (Washington GPO)

Boulanger F., Falgarone E., Puget J.L., Helou G., 1990, ApJ 364, 136

Boulanger F., Bronfman L., Koprucu M., Thaddeus P., 1992, in preparation

Cernicharo J., Bachiller R., 1984, A&A sup 58, 327

Chlewicky G., Laureijs R.J., 1988, A&A (Letters) 207, L11

Flannery B.P., Roberge W., Rybicki G., 1980, ApJ 236, 598-608

Désert X., Boulanger F., Puget J.L., 1990, A&A 237, 215 (DBP)

Draine B.T., Anderson N., 1985, ApJ 292, 494

Giard M., Pajot F., Lamarre J.M., Serra G., Caux E., 1989, A&A 215, 92

Helou G., Ryter C., Soifer B.T., 1991, In press

Langer W.D., Wilson R.W., Goldsmith P.F., Beichman C.A., 1989, ApJ 337, 355

Laureijs R.J., Clarck F. O., Prusti T., 1991, ApJ 372, 185

Laureijs R.J., Chlewicki F.O., Clark F.O., Wesselius P.R., 1989, A&A 220, 226 (LCCW)

Lillie C.F., Witt A.N., 1976, ApJ 208, 64

Léger et al. 1989 Proceedings of the I.A.U. Symposium 135 on the interstellar dust, Eds L.J. Allamandola and A.G.G.M. Tielens, (Washington GPO)

Léger A., Puget J.L., 1984, A&A 137, L5

Lis D.C., Leung C.M., 1991, Icarus 91, 7 (LL)

Mathis J.S., Rumpl N., Nordsieck K.H., 1977, ApJ 217, 425

Mathis J.S., Mezger P.G., Panagia N., 1983, A&A 128, 212 (MMP)

Pérault M., Boulanger F., Falgarone E., Puget J.L., 1989, ApJ submitted

Puget J.L., 1989, Interstellar Dust Eds L.J. Allamandola and A.G.G.M. Tielens, p119

This article was processed by the author using Springer-Verlag LaTeX A&A style file 1990.